

Novel Physics of Escaping Secondary Atmospheres May Shape the Cosmic Shoreline

RICHARD D. CHATTERJEE¹ AND RAYMOND T. PIERREHUMBERT¹¹ *Atmospheric, Oceanic and Planetary Physics, University of Oxford*

ABSTRACT

Recent James Webb Space Telescope observations of cool, rocky exoplanets reveal a probable lack of thick atmospheres, suggesting prevalent escape of the ‘secondary’ atmospheres formed after losing primordial hydrogen. Yet, simulations indicate that hydrodynamic escape of secondary atmospheres, composed of nitrogen and carbon dioxide, requires intense fluxes of ionizing radiation (XUV) to overcome the effects of high molecular weight and efficient line cooling. This transonic outflow of hot, ionized metals (not hydrogen) presents a novel astrophysical regime ripe for exploration. We introduce an analytic framework to determine which planets retain or lose their atmospheres, positioning them on either side of the cosmic shoreline. We model the radial structure of escaping atmospheres as polytropic expansions—power-law relationships between density and temperature driven by local XUV heating. Our approach diagnoses line cooling with a three-level atom model and incorporates how ion-electron interactions reduce mean molecular weight. Crucially, hydrodynamic escape onsets for a threshold XUV flux dependent upon the atmosphere’s gravitational binding. Ensuing escape rates either scale linearly with XUV flux when weakly ionized (energy-limited) or are controlled by a collisional-radiative thermostat when strongly ionized. Thus, airlessness is determined by whether the XUV flux surpasses the critical threshold during the star’s active periods, accounting for expendable primordial hydrogen and revival by volcanism. We explore atmospheric escape from Young-Sun Mars and Earth, LHS-1140 b and c, and TRAPPIST-1 b. Our modeling characterizes the bottleneck of atmospheric loss on the occurrence of observable Earth-like habitats and offers analytic tools for future studies.

Keywords: Analytical mathematics (38), Astrophysical fluid dynamics (101), Aurorae (2192), Exoplanet atmospheric evolution (2308), Habitable planets (695), Star-planet interactions (2177)

1. INTRODUCTION

The circumstellar habitable zone is traditionally defined as where planets are cool enough to host liquid water (Huang 1959), but other conditions must be fulfilled to retain a suitable atmosphere. Making up > 70% of the stars in the Milky Way are the low-mass M-dwarfs, which host at least one small planet on average (Dressing & Charbonneau 2015). Low mass stars often do not spin down appreciably, meaning their ionizing luminosity can be one part in a thousand of their bolometric (total) luminosity for billions of years (Fleming et al. 2020). For the population of planets companion to active stars, the open problem of what atmospheres

will survive has risen in prominence due to the 2021 launch of the *James Webb Space Telescope* with its capability to observe cool rocky planets in transmission and emission. Indeed, *JWST* observations of the two closest-in planets of the now pre-eminent TRAPPIST-1 system (Gillon et al. 2017; Greene et al. 2023; Zieba et al. 2023) were consistent with bare rocks. If planets such as TRAPPIST-1 b and c are confirmed to be airless, is the most compelling explanation then a volatile-poor birth or catastrophic photoevaporation?

Meeting the conditions for the hydrodynamic escape of secondary atmospheres may divide the airless from the airy rocky exoplanet populations, metaphorically described as the Cosmic Shoreline (Zahnle & Catling 2017). Secondary atmospheres can form in the continuous transition from an escaping nebular atmosphere, evolve from an initial high-molecular-weight at-

mosphere, or are revived by volcanism from a bare rock (e.g., Kite & Barnett 2020; Krissansen-Totton et al. 2024). We focus on modeling the retention of nitrogen-dominated atmospheres because this is crucial for assessing the potential for Earth-like habitats orbiting M-dwarfs (Lammer et al. 2019). The physics governing the escape of CO₂-dominated atmospheres is similar but differences arise due to infrared cooling lines and photochemistry (e.g., Tian 2009; Van Looveren et al. 2024). Though some insight can be carried over to the escape of steam-dominated atmospheres, the shift in dynamics due to the hydrogen ions in the upper atmosphere is outside the scope of the present study and we refer the reader to the literature devoted to this topic (e.g., Johnstone 2020; Yoshida et al. 2022; García Muñoz et al. 2024).

Due to its high molecular weight and efficient cooling by atomic lines, escaping a secondary atmosphere requires a large flux of stellar irradiation with a shorter wavelength than the hydrogen ionization edge: extreme ultraviolet (10-92 nm) and X-ray (0.1-10 nm). The strong and broad XUV photoabsorption cross-section finds the tenuous gas of the planet’s infrared photosphere optically thick and efficiently drives a temperature inversion from the hot electrons and atoms released. That is in contrast to the lower atmosphere, where heat from photoabsorption is efficiently reradiated as a black-body to space, so it cannot contribute to escape. The work reported here constrains the threshold XUV fluxes for evolution to airlessness for the size range of rocky exoplanets.

1.1. Hydrostatic versus Hydrodynamic

The easier escape of hydrogen compared to nitrogen, or other metals, can be marked out through the two limits of thermal atmospheric loss: Jeans and hydrodynamic (Fig 1). Jeans escape occurs at the exobase of a hydrostatic atmosphere, where collisions are infrequent, so the minor fraction of particles that are thermally endowed with the local escape velocity can be ballistically ejected to space (Jeans 1921). However, for significant depletion over millions of years, a mechanism of bulk escape is required. The atmosphere can flow into the interplanetary medium as a steady hydrodynamic wind, reaching supersonic speeds analogous to the solar wind predicted by Parker (1958). At the sonic point r_{sc} , the velocity must roughly equal half the local escape velocity v_{esc} . So, greater gravitational acceleration $g(r)$ or higher mean molecular mass μ of the flow requires higher atmospheric temperatures because $T_{sc} \propto g(r_{sc})r_{sc}\mu$.

Atmospheric escape from Earth for an atomic nitrogen sonic flow requires a temperature of roughly 15 000 K,

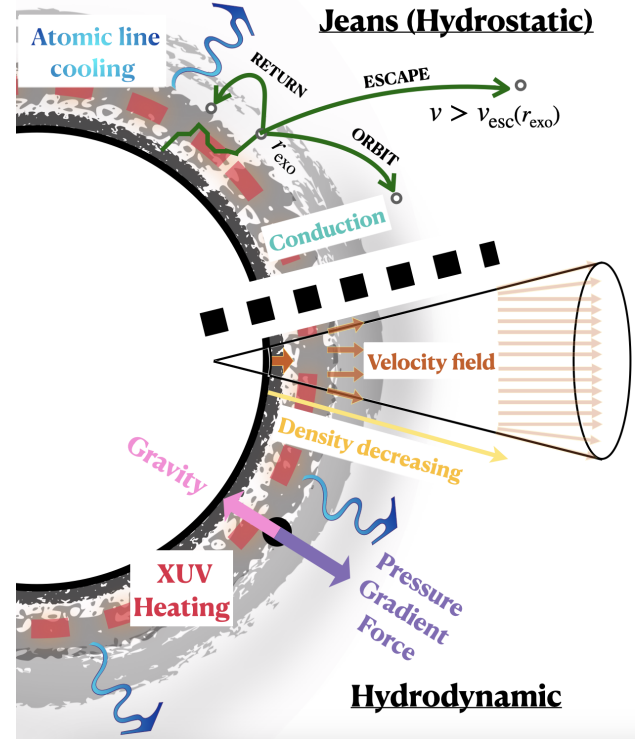


Figure 1: Illustration comparing hydrodynamic and hydrostatic escape of a secondary atmosphere (not to scale). In hydrodynamic escape, the net heating from XUV photoabsorption, reduced by recombination and atomic line cooling, drives a pressure gradient force to overcome gravity— accelerating the flow radially outwards down the atmosphere’s density gradient. Jeans escape occurs from the hydrostatic exobase where the atmosphere becomes collisionless. If the thermal velocity of a particle directed outwards exceeds the escape velocity v_{esc} at the exobase radius r_{exo} , then it can ballistically escape on a hyperbolic trajectory. The balance of XUV heating, conduction, and line cooling determines the escape rate via the exobase temperature.

while for atomic hydrogen less than 1000 K is sufficient. The complementary perspective is that a hydrostatic exobase cannot remain in equilibrium for a large rate of Jeans escape, which increases exponentially with temperature. When the sound speed reaches roughly half the escape velocity, the supply to the exobase shifts from diffusion to in-bulk. Tian et al. (2008) calculated that the exobase of a primordial hydrogen atmosphere on Earth would collapse at temperatures around 500 K compared to 7000 K for a composition of atomic nitrogen and oxygen.

So that the pressure gradient force can accelerate an outflow to sound speed, the flow must remain collisional— the exobase should be above the sonic al-

titude. There is a corresponding threshold in XUV flux to meet this Knudsen onset, which we name after the onset after the dimensionless number for collisionality (Knudsen 1909). With increasing ionization, the rapid Coulomb collisions make the Knudsen-onset less restrictive. The general increase in escape with the higher temperatures generated by a greater XUV flux limits the ionization fractions in an upper atmosphere. However, ions and electrons can still dominate if XUV heating can be efficiently radiated away. Ambipolar motion will also reduce the temperatures required for rapid escape: the Coulomb attraction of the electrons drags out the ions, effectively halving their mean molecular weight and so doubling their scale height (Bauer & Lammer 2004). Earth’s ambipolar electrostatic field was recently measured in-situ for the first time by the Endurance rocket (Collinson et al. 2024). The debated protective effects of planetary magnetic fields are beyond the scope of the present study.

1.2. Radiative Cooling: Hydrogen versus Metal

The photoevaporation of secondary atmospheres represents a novel astrophysical regime in that it is a ‘metal’ flow— not dominated by hydrogen. The hydrodynamic escape of hydrogen atmospheres has been observed from Hot Jupiters since Vidal-Madjar et al. (2003, 2004) and theoretical modelling was used to predict the bimodality in the radius distribution of sub-Neptunes (Owen & Wu 2013; Lopez & Fortney 2013; Fulton et al. 2017). For evaporation of hydrogen envelopes from close-in giant planets, XUV heating competes with cooling from electron-impact excitation of the $\text{HI}_{\text{Ly}\alpha}$ emission from 10.2 eV above ground and by radiative recombination of ions with electrons (e.g., Murray-Clay et al. 2009).

Groundbreaking simulations by Nakayama et al. (2022) demonstrated that cooling via collisional excitation of the metastable states of N, C, and O—each with excitation energies around 1 eV to 4 eV, making them more accessible than $\text{HI}_{\text{Ly}\alpha}$ —was sufficient to maintain temperatures low enough for an Earth-like atmosphere to remain hydrostatic under $1000\times$ current Solar XUV flux. Their inclusion of efficient atomic cooling revised the resistance of Earth’s atmosphere to XUV-driven hydrodynamic escape by orders of magnitude (Tian et al. 2008) and offers more favorable prospects for Earth-sized exoplanets orbiting M-dwarfs retaining atmospheres. However, the present study reports that the assessment of Jeans escape by Nakayama et al. (2022) to determine hydrostatic instability only partially accounts for the increasing ionization of the neutral exobase and neglects the eventual supplanting by the ion exobase.

We also note that consistency of the unexplored hydrodynamic equilibrium is not necessarily mutually exclusive with a consistent hydrostatic equilibrium as they occupy different regimes: ionization-recombination and ionization-advection balances, respectively. We will first explore predominantly neutral hydrodynamic escape and then introduce a new regime of global ion outflow controlled by a collisional-radiative thermostat. This thermostatic feedback, which can be inferred from the simulations of Nakayama et al. (2022), can be compared to that due to line cooling of minor-abundance metals in a photoionisation-equilibrated hydrogen flow such as found in stellar winds (Drew 1985), planetary nebula (Seaton 1960) and even galaxy clusters (Ferland et al. 2009).

1.3. Analytic and Numerical Modeling

Johnstone et al. (2019) time-stepped the discretised multispecies Navier-Stokes Equations with radiative transfer and photochemistry to solve for the steady-state escape of Earth’s atmosphere under the raised XUV output of the Young Sun. This approach, henceforth referred to as a hydrocode, is the most comprehensive. However, its conclusions are still vulnerable to neglected physics, which in this case was the forbidden line cooling later found to be important by Nakayama et al. (2022), and the computational expense is prohibitive for broader studies. At the opposite end of complexity, there is the energy-limited parameterization, adapted from Watson et al. (1981), which calculates the mass loss rate via the total XUV heating needed to accelerate atmospheric layers to escape velocity with some fixed efficiency.

The work reported here uses a polytropic approximation for the atmospheric structure to bridge the modeling gap:

$$\left(\frac{\rho}{\rho_0}\right)^{\gamma-1} = \frac{T}{T_0}, \quad 0 < \gamma \leq \gamma_a, \quad (1)$$

comparing the density ρ and temperature T to reference values (ρ_0, T_0) , for example, at the thermobase. By varying the polytropic index γ between adiabatic expansion γ_a (e.g. monatomic $\gamma_a = 5/3$), Parker’s isothermal wind $\gamma = 1$, and thermal inversions $\gamma < 1$, we unify a range of idealized planetary outflows. The polytropic equation of state is widely used but is best known for solutions to stellar structure (e.g., Chandrasekhar 1931). We adopt and generalize results from application of polytropes to the transonic solar wind, including the exact algebraic solution to the dimensionless problem from Holzer & Axford (1970) and extend approximations to the dimensional problem from Lamers & Cassinelli (1999).

The other dimensionless parameter required to define polytropic solutions is the hydrodynamic escape parameter λ_0 , which is the ratio of gravitational to thermal energy at the base of the flow. We show that $\lambda_0 \gg 1$ for high-molecular-weight atmospheres allows a priori specification of the sonic altitude and the base-to-sonic ratios of flow properties. Owen & Jackson (2012) use a polytropic model for hydrogen outflow from close-in hot Jupiters with $\lambda_0 \rightarrow \infty$ and γ set by the slope of the photoionization equilibrium function. We show how γ determines the profile of local polytropic heating to drive a given steepness of thermospheric inversion and relate γ to the XUV flux given a fixed λ_0 . Owen & Jackson (2012) extended their model to an altitude-dependent γ via a pretabulated function; such a formulation may not be possible for metal outflows and is not explored in the present study.

Johnson et al. (2013a,b) numerically solved the Boltzmann equation for flow through the exobase with Direct Simulation of particles and collisions via a Monte Carlo algorithm (DSMC, Bird 1994). Exploring the transition from subsonic escape, Johnson et al. (2013a,b) developed an analytic criterion for the minimum XUV heating to drive transonic outflow. We draw further insight from the polytropic model by computing the atmospheric structure entailed by the Knudsen onset. For collisional flow up to the sonic point launched from a base characterized by λ_0 , the Knudsen onset polytropic index γ_{on} yields a threshold in XUV flux. We provide analytic expressions for the global thermomechanical efficiency and scale height at the sonic point. Atomic line emission finds the thermosphere optically thin, so we use a three-level atom model to analytically calculate cooling direct to space. When the cooling is found to exceed the polytropic heating in the Knudsen onset, conditions are not favorable for allowing predominantly neutral outflow. The limit of high XUV flux may instead drives global ion outflow under the collisional radiative thermostat.

1.4. Structure of the Paper

For the application of the polytropic framework and our other analytic models, we explore Young Sun XUV-evaporation of nitrogen atmospheres from Earth and Mars, as well as prospects of atmospheric retention around M-dwarfs in the cases of Earth-sized TRAPPIST-1 b and super-Earths LHS-1140 c and b. The remainder of the paper is organized as follows:

Section 2 derives and characterizes the solution space for escaping planetary atmospheres under a polytropic equation of state that can be related to XUV heating. Section 3 demonstrates how the Knudsen onset in col-

lisional determines a unique polytropic solution, establishing a threshold XUV flux required to sustain predominantly neutral transonic outflow of high molecular weight atmospheres. Section 4 introduces the three-level atom model for electron-impact excitation of forbidden lines, emphasizing its role in the energetics of the neutral Knudsen onset during transonic escape. Section 5 explores whether atomic line cooling can protect a hydrostatic atmosphere from instability under a rising XUV flux producing more ions in the upper atmosphere as relevant to Nakayama et al. (2022). This leads us to introduce the regime of global ion outflow from super-Earths, where Coulomb collisions sustain pressure gradients within tenuous outflows, establishing alternative XUV-flux thresholds dictated by thermostat-limited escape. Section 6 integrates these findings to examine the broader landscape of high-molecular-weight atmospheric escape and its implications for the cosmic shoreline of rocky exoplanets. Our conclusions are summarized in Section 7.

2. POLYTROPIC MODEL OF ATMOSPHERIC ESCAPE

A compressible fluid in 1D requires four equations to solve for four unknowns: transport of mass, momentum, and energy, with an equation of state to calculate density, pressure, velocity, and temperature. The polytropic relation (Eqn 3) takes the place of the momentum equation. However, the momentum equation is still key to understanding the flow solution. In this section, we build on previous work to derive an analytic solution space for the structure of escaping atmospheres.

2.1. Character of XUV-driven Transonic Expansion into Space

A planetary atmosphere driven by XUV heating to expands outward from the thermobase can meet the stellar wind and match its dynamic pressure, yielding a subsonic breeze with mass loss proportional to the ‘inlet-outlet’ pressure difference. Continuously reducing the pressure imposed by the stellar wind allows further outward acceleration of the atmosphere driven by the pressure gradient until the flow becomes supersonic at a critical pressure. Once the flow is transonic, the mass loss rate has reached a maximum independent of the upper boundary conditions: any forcing downstream of the sonic altitude cannot influence the upstream flow (Pierrehumbert 2010). A subsonic breeze transporting gas up to the exobase is also possible, yielding ballistic escape from a drifting-Maxwellian (Volkov 2011), but we set that case aside on noting it would still respect the upper bound of the transonic rate.

The spherically symmetric steady-state compressible Euler Equations equations admit a range of flow solutions in a gravitational field, illustrated in the Mach-radius phase plane ($M = 1$) in Figure 2. The integral curves form a saddle geometry centred around the sonic point: $M = 1$, $u_{sc} = \sqrt{fRT_{sc}}$, $r = r_{sc}$, where f is an order unity dimensionless prefactor, and R is the specific gas constant. An aid to interpreting the geometry is that a flow can time-evolve to occupy different parts of the solution curves for accretion and escape through a hysteresis loop (Velli 1994).

The mass flux of the outflow must be radially uniform, and the momentum equation can then be written as a compressibility-weighted acceleration outwards, provided by a pressure-gradient force split into an adiabatic and a diabatic component:

$$(u^2 - c_a^2) \frac{1}{u} \frac{du}{dr} = \frac{2c_a^2}{r^2} \left(r - \frac{GM}{2c_a^2} \right) - (\gamma_a - 1) 4\pi r^2 q_v, \quad (2)$$

with radius r , radial velocity u , adiabatic sound speed $c_a = \sqrt{\gamma_a RT}$, net volumetric heating rate q_v , density ρ , and planet mass M .

For volumetric heating prescribed as a function of radius only, the velocity gradient is unbounded where the flow velocity equals the adiabatic sound speed unless the radius satisfies $r_{sc} = GM/2u_{sc,a}^2$. However, $q_v(r)$ is not representative of planetary atmospheres: if the flow is perturbed, the density changes, which would displace the distribution of stellar heating such that heating is implicitly also a function of the velocity gradient. To find the sonic point for $q_v(r, \frac{du}{dr})$ in general, if one exists at all, the energy and momentum equations can be written as an autonomous system of decoupled first-order ODEs (Bauer & Carter 2021). The central reduction of the present study is to an approximately polytropic atmospheric structure, given by

$$\left(\frac{\rho}{\rho_0} \right)^{\gamma-1} = \frac{T}{T_0}, \quad u_{sc} = \sqrt{\gamma RT_{sc}} \text{ \& } r_{sc} = \frac{GM}{2u_{sc}^2}. \quad (3)$$

This equation generalises from the $\gamma = \gamma_a$ adiabatic expansion to a polytropic expansion where $0 < \gamma < \gamma_a$, corresponding to implicit inclusion of distributed heating given by

$$q_\gamma \cdot 4\pi r^2 \rho = \Phi_{\text{hyd}} \cdot \left(\frac{\gamma_a}{\gamma_a - 1} + \frac{\gamma}{1 - \gamma} \right) R \frac{dT}{dr}, \quad (4)$$

where Φ_{hyd} is the mass loss rate and q_γ is the polytropic model's implicit specific heating per unit mass. The polytropic solution ($\Gamma = \gamma$) will be consistent with an

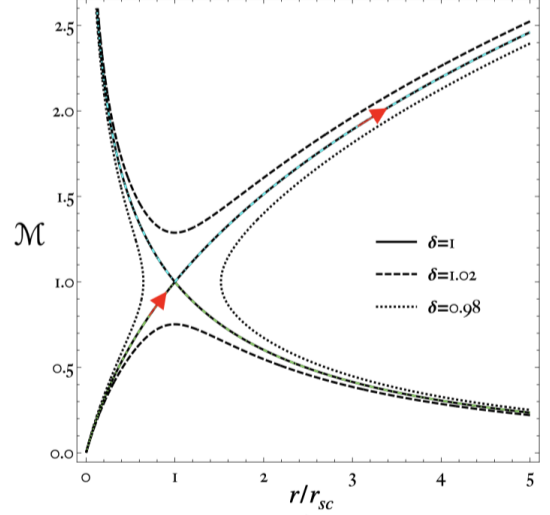


Figure 2: Contour plot of Mach number M against dimensionless radius r/r_{sc} for a diatomic adiabatic expansion ($\gamma_a = 1.4$) example solutions: transonic ($\delta = 1$), subsonic/supersonic ($\delta = 1.02$), and double-valued ($\delta = 0.98$). The transonic escape solution is highlighted with red arrows. The transonic contours' upper and lower branches are highlighted with a dot-dashed line of cyan and green, respectively. δ relates to the entropy differences between different types of solutions (see Eqn 10).

diabatic-driven ($\Gamma = \gamma_a$) solution at each altitude:

$$\Phi_{\text{hyd}} \cdot \frac{d}{dr} \left(\frac{u^2}{2} + \frac{c_\Gamma^2}{\Gamma - 1} - \frac{GM}{r} \right) = \begin{cases} 4\pi r^2 \rho q & : \Gamma = \gamma_a \\ 0 & : \Gamma = \gamma, \end{cases} \quad (5)$$

if $q = q_\gamma$. The differently framed flows have the same velocity and gravitational potential but different internal energies. The physical interpretation of Eqns (4 & 5) is that the total heating in each local spherical shell drives the transport of specific internal energy at each altitude. The shift of the saddle point from the adiabatic u/c_a to the polytropic Mach number u/c_γ is due to a regularising perturbation from the imposition of polytropic heating, as the temperature becomes implicitly dependent on the velocity gradient through the implicit heating. This shift in the sonic point is comparable to that from conduction regularization (e.g., Hong et al. 2014). Note that the classic analytic solution of the isothermal Parker Wind also requires implicit heating to accelerate the flow, which the XUV section of stellar irradiation often provides.

A hydrodynamic upper atmosphere, not limited by the supply of the escaping component from the lower atmosphere, will often escape limited by the energy input

(e.g., [Watson et al. 1981](#)). The absorbed stellar XUV lifts gas out of the planet's gravitational well with an efficiency η :

$$\Phi_{\text{hyd}} \frac{GM_p}{r_0} = \eta \cdot \pi r_{\text{abs}}^2 \frac{\mathcal{L}_{\text{XUV}}}{4\pi a^2}, \quad (6)$$

where the planet's surface radius is r_0 , orbiting with semi-major axis a ; \mathcal{L}_{XUV} is the star's XUV luminosity with a peak absorption at planetary radius r_{abs} . In the energy-limited parametrization, a physics-based derivation of η and r_{abs} is neglected. We address two of the major limitations of the energy-limited parametrization ([Gronoff et al. 2020](#)) by evaluating the escape regime via the Knudsen onset and evaluating the atmospheric profiles with polytropic solutions. For hydrogen escape, an alternative prescription for advancing beyond the ELP used a grid of hydrocode models to construct fits for mass loss rates ([Kubyshkina et al. 2018](#)).

The present study breaks down the efficiency η into a product of the thermomechanical, photoreaction and cooling efficiencies:

$$\eta = \eta_\gamma \eta_{\text{pr}} \eta_c, \quad (7a)$$

$$\eta_\gamma \approx \frac{2\gamma r_{\text{sc}}}{r_0} \left(\frac{\gamma_a}{\gamma_a - 1} + \frac{\gamma}{1 - \gamma} \right)^{-1} \quad (7b)$$

The thermo-mechanical η_γ efficiency of polytropic escape is derived by integrating the implicit heating up to the sonic point (Eqn 4) and comparing to the heating needed to lift the mass out of the gravitational well. The thermal energy at the base is neglected, so Equation (7b) is approximate, but an exact comparison as a function of the boundary conditions is straightforward. The photoreaction efficiency accounts for the excess energies of photoionisation and photodissociation. The cooling efficiency represents how much of the available XUV-heating is converted into line cooling from the thermosphere. It can be evaluated analytically with altitude on the polytropic profiles as will be explored in Sections 3.2 and 4.

2.2. Polytropic Approximation to Atmospheric Structure and Escape

Polytropic atmospheric structure spans a range of idealized hydrostatic and hydrodynamic vertical equilibria. [Holzer & Axford \(1970\)](#), following on from the work of Parker, provided an algebraic solution to the dimensionless problem for the polytropic solar wind. Our work extends the calculation to solve the dimensional problem, folding it into the framework for high-molecular-weight transonic escape of planetary atmospheres. Conservation of mass and the Bernoulli equation for energy link

the sonic flow properties to the rest of the flow as:

$$\rho u r^2 = \rho_{\text{sc}} u_{\text{sc}} r_{\text{sc}}^2, \quad (8a)$$

$$\frac{u^2}{2} + \frac{c^2}{\gamma - 1} - \frac{GM}{r} = \left(\frac{5 - 3\gamma}{\gamma - 1} \right) \frac{u_{\text{sc}}^2}{2}, \quad (8b)$$

where we have simplified the energy at the sonic point using Equation (3). This pair of equations can be expressed in terms of two unknowns, the Mach number $\mathcal{M} = u/c_\gamma$ and dimensionless radius $\xi = r/r_{\text{sc}}$, yielding

$$\left(\frac{c^2}{u_{\text{sc}}^2} \right)^{\frac{\gamma+1}{\gamma-1}} \mathcal{M}^2 \xi^4 = 1, \quad (9a)$$

$$\frac{c^2}{u_{\text{sc}}^2} \left(\frac{\mathcal{M}^2}{2} + \frac{1}{\gamma - 1} \right) = \frac{1}{2} \left(\frac{5 - 3\gamma}{\gamma - 1} \right) + \frac{2}{\xi}. \quad (9b)$$

To find the implicit algebraic solution, $\frac{c^2}{u_{\text{sc}}^2}$ can be eliminated from Equation (9b) by substitution of Equation (9a). The governing equation

$$2\delta \left(\frac{1}{\gamma - 1} + \frac{\mathcal{M}^2}{2} \right) (\mathcal{M}^2)^{-\frac{\gamma-1}{\gamma+1}} = \left(\frac{5 - 3\gamma}{\gamma - 1} + \frac{4}{\xi} \right) \xi^{4(\frac{\gamma-1}{\gamma+1})} \quad (10)$$

can be found numerically as a contour, where the transonic outflow is selected from amongst accretion and multivalued solutions (Fig 2) via specifying a constant of integration $\delta = 1$ ([Holzer & Axford 1970](#)). Related to entropy, we have reinserted δ so that Equation (10) is in its most general form. The form of solution mirrors the isothermal Parker Wind, except that most scientific computational libraries have a pre-tabulated function for the Parker contours, called the Lambert W-Function ([Cranmer 2004](#)). Equation (10) also recovers the isothermal solution in the limit $\gamma \rightarrow 1$ with the Bernoulli definition of the exponential; see discussion of Equation (20).

The above solution for the Mach profile is the seed for the solution to all other profiles. To calculate the dimensionless temperature, conservation of mass (Eqn 9a) can be used directly. The temperature profile can be fed into the polytropic relationship (Eqn 3) to determine the dimensionless density profile. Lastly, a combination of the temperature and Mach number profiles yields the dimensionless velocity profile via energy conservation (Eqn 9b).

The hydrodynamic escape parameter is defined as is the ratio of gravitational energy to thermal energy at the base of the flow (e.g., [Watson et al. 1981](#)):

$$\lambda(r_0) = \lambda_0 = \frac{GM}{RT_0 r_0} \quad (11)$$

and is the other dimensionless parameter for the polytropic model. We will refer to an escape temperature

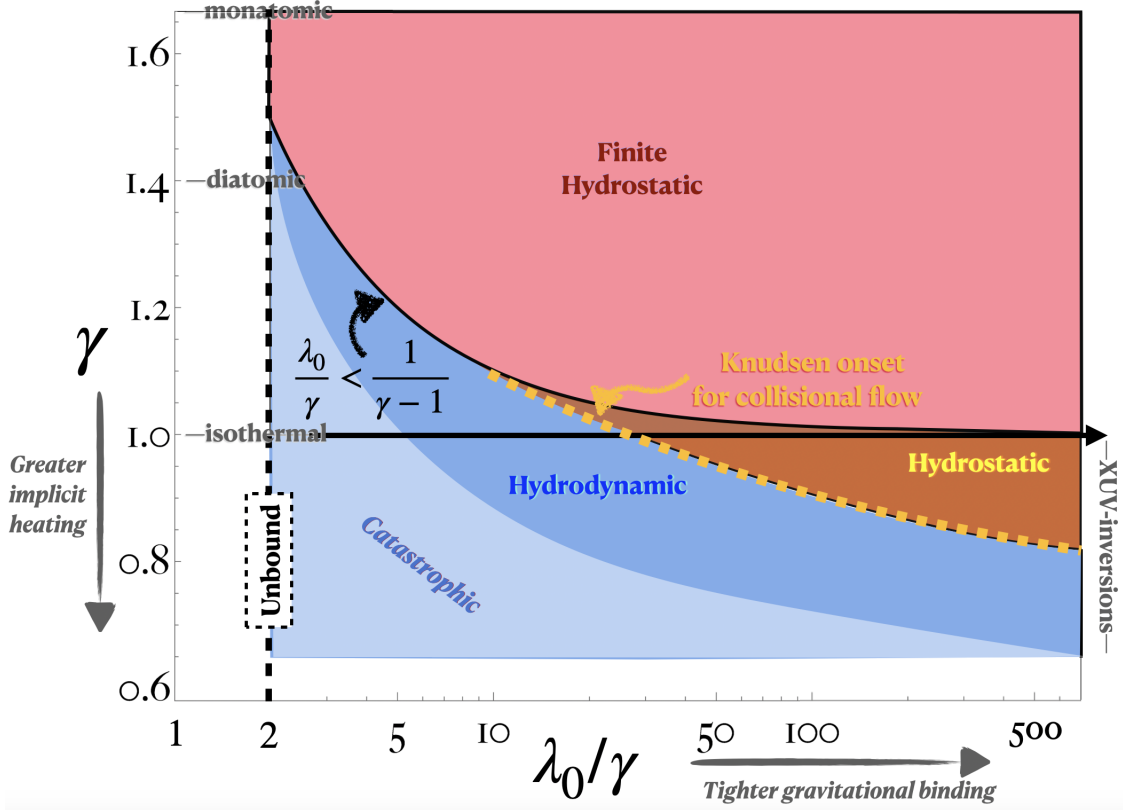


Figure 3: Steady-state polytropic solutions space for vertical atmospheric equilibrium. For $\frac{\lambda_0}{\gamma} > \frac{1}{\gamma-1}$, the equilibrium is hydrostatic with density reaching zero at a finite height (pink). Implicit heating throughout the atmosphere reduces γ from an adiabat γ_a . For $2 < \frac{\lambda_0}{\gamma} < \frac{1}{\gamma-1}$, the thermal energy at the base in addition to the implicit heating is large enough to drive an accelerating transonic flow in principle (blue hydrodynamic region). The supersonic at the base constraint $\lambda_0 = 2$ is represented by the dashed vertical line and labelled ‘unbound’. The blue region of consistent steady state does not extend all the way to this line, however, because the flow launch should have $\mathcal{M} \ll 1$, otherwise the escape is ‘catastrophic’ (light blue). On failure of the hydrodynamic assumption at the sonic point, XUV-driven inversions ($\gamma < 1$) give way to hydrostatic atmospheres that would be infinite except for the formation of an exobase (brown region). The yellow line is then the Knudsen onset for collisional flow given by $\text{Kn}_{sc}^N \sim 1$ (see Section 3).

analogous to the concept from protoplanetary disc photoevaporation (e.g., Owen & Jackson 2012). It is defined as the temperature necessary at some altitude for the isothermal sound speed to equal half the escape velocity, or equivalently, $\lambda(r) = 2$:

$$T_{\text{esc}}(r) = \frac{\mu}{4k_B} v_{\text{esc}}(r)^2. \quad (12)$$

At the escape temperature, the sonic point of an isothermal hydrodynamic flow would be reached (Pierrehumbert 2010), while if the top of a hydrostatic atmosphere were at this temperature it would collapse into a blow-off state (Öpik 1963). Moreover, if the temperature at the exobase is a half to a third of the escape temperature, a hydrostatic equilibrium would be unstable and expand hydrodynamically (Tian et al. 2008).

Although these profiles can hypothetically be calculated for a planetary atmosphere with any (γ, λ_0) , to

describe well a steady state, the planetary wind should launch highly subsonic. Thus, the \mathcal{M}^2 term in energy conservation can be neglected to provide a simple approximation for the sonic radius, where

$$\xi_0 \approx \frac{\frac{4\gamma}{\lambda_0} - 4(\gamma - 1)}{5 - 3\gamma} = \xi_0^{\text{itr},1}, \quad (13)$$

specifying the dimensional profile and collapsing the degeneracy in the sonic point through a single iteration in the first approximation $\xi_0^{\text{itr},1}$. In the context of flows which start with appreciable Mach numbers, one can find the $\mathcal{M}_{\text{itr},1}^2$ via the Equations (13 & 10), to find the second approximation, given by

$$\xi_0^{\text{itr},2} = \frac{\frac{4\gamma}{\lambda_0} \left(\frac{1}{2} \mathcal{M}_{\text{itr},1}^2 + \frac{1}{\gamma-1} \right) - 4}{\frac{5-3\gamma}{\gamma-1}}. \quad (14)$$

This allows full specification of, for example, adiabatic diatomic expansion, usually after only one iteration.

The equations for the sonic point radius can be compared to Equation (13) from [Owen & Jackson \(2012\)](#), which assumed $\gamma < 1$, $\lambda_0 \rightarrow \infty$.

Neatly, the approximate mass flux can be found immediately using the first iteration (Eqn 13) - without needing to compute the contour. The mass loss rate, given by $4\pi\rho ur^2$ and expressed in terms of γ , λ_0 and the lower boundary, becomes

$$\Phi_{\text{hyd}} = 4\pi\rho_0 r_0^2 \left(\frac{v_{\text{esc}}(r_0)}{2} \right) \left(\frac{\lambda_0}{2\gamma} \right)^{1/(\gamma-1)} \times \left(\frac{4\gamma/\lambda_0 - 4(\gamma-1)}{5-3\gamma} \right)^{\frac{5-3\gamma}{2(\gamma-1)}}. \quad (15)$$

Lastly, Equation (13) allows simple determination of all sonic-to-base ratios for flow launching highly subsonic:

$$\frac{T_{sc}}{T_0} = \frac{\lambda_0 \xi_0}{2\gamma}, \quad (16a)$$

$$\frac{\rho_{sc}}{\rho_0} = \left(\frac{T_{sc}}{T_0} \right)^{1/(\gamma-1)} \quad (16b)$$

$$\frac{u_{sc}}{u_0} = \frac{\rho_0}{\rho_{sc}} \xi_0^2. \quad (16c)$$

2.3. Polytropic Solution Space

Figure 3 presents the solution space of vertical equilibrium for polytropic atmospheres. We devote significant discussion to the space of regions in (γ, λ_0) so that Figure 3 can be used as a touchpoint to understand idealized solutions to escape. It is instructive to follow the thermodynamic expansion of a parcel lifted through the atmosphere.

For $\lambda_0/\gamma > 1/(\gamma-1)$, the sum of the thermal energy at the base with the integrated heating is insufficient to give the parcel enough energy to escape the planet's gravitational well so that the atmosphere will be hydrostatic. An air parcel will cool as it rises, and its density will tend to zero on reaching a finite terminus of the atmosphere. The cooling will be less for $\gamma \rightarrow 1$, where $\gamma < \gamma_a$ entails implicit heating throughout the atmosphere. The pink region of Figure 3 thus marks where only a finite hydrostatic atmosphere is consistent.

Moving leftwards, the blue region $\lambda_0/\gamma < 1/(\gamma-1)$ in Figure 3 marks where transonic escape solutions exist, and finite hydrostatic atmospheres are inconsistent. There are no consistent hydrodynamic escape solutions for $\gamma > 3/2$, as such flows would be decelerating from the base and only preserve uniform mass transport outwards because the spherical surface area increases with the radius. The $\gamma = 1.4$ diatomic adiabatic expansion permits an accelerating transonic solution with an unrealistic velocity profile. The near field limit $\xi \ll 1$

of Equation (10) combined with Equation (9a) yields $u_0/u_{sc} \approx 1.3\sqrt{\mathcal{M}_0} = \sqrt{2\xi_0}$, so that even as far out as $r_{sc} = 40r_0$, which allows $\mathcal{M}_0 = 1/20$, the sonic velocity is only $3\times$ the base velocity in the diatomic case. Then, the atmosphere above the base is lost on the timescale of days.

Reducing γ down towards 1 through the implicit imposition of heating allows the flow to be driven from a lower temperature base and for acceleration to sonic velocity orders of magnitude greater than base velocity, yielding loss timescales for the thermosphere on a timescale of thousands of years or more. The lower atmosphere replenishes the thermosphere so that a quasi-steady state hydrodynamic escape solution can proceed on a loss timescale of a million years, where the atmospheric pressure decreases or there is a balance with outgassing.

In an isothermal expansion $\gamma = 1$, the gas does work but heat flows in to keep the temperature the same. For $\gamma < 1$, a rising parcel heats as it expands up a thermospheric inversion due to the implicit heating outweighing adiabatic cooling. The model mass loss then increases linearly with the XUV flux, apart from a small variation in the thermomechanical efficiency, consistent with the energy limit.

Two exceptional regions show where mass loss is catastrophically fast in light blue and where the hypothetical flow becomes collisionless before reaching sound speed in brown. The catastrophic region begins where an atmosphere would be unbound at $\lambda_0 \leq 2$. Even for higher λ_0 , increasing XUV flux reduces γ so that sound speed is reached in a dense layer (Eqn 16b), yielding too-rapid mass loss for a valid steady state of a planetary atmosphere. In the limit of large λ_0 , a hydrodynamic atmosphere would find the exobase below the hypothetical sonic altitude. The Knudsen onset (yellow-line), which will be discussed in detail in the following section, entails a minimum steepness of polytropic inversion γ_{on} , which must be generated by a threshold XUV flux to drive transonic hydrodynamic escape.

2.4. Where is the Base?

The role of lower boundary conditions varies with the polytropic index. For adiabatic thermally driven escape, any gas at the bottom of the potential well has enough thermal energy to escape, so the mass loss is set by the base density. Similarly, isothermal planetary winds are set by lower-boundary assumptions with large uncertainties and degenerate scenarios arise; see core-powered mass loss (e.g., [Tang et al. 2024](#)). Steep inversions ($\gamma < 1$) are the only analytic solutions that are consistent with the dynamics of the energy limit.

The densities in the flow (base or sonic) are restricted to yield a mass loss less than the XUV heating available. We adopt mesopause-like densities for the lower boundary of secondary atmospheres. We note that a spectrum richer in shorter wavelengths will launch the flow from deeper into the atmosphere, all else being equal. As will be discussed in Section 3.2.2, on varying the base density by an order of magnitude, the profiles are only moderately sensitive and the mass loss rate quite insensitive within the error already anticipated in an analytic approximation.

3. XUV-FLUX THRESHOLD FOR TRANSONIC ESCAPE

In this section, we will calculate whether there is an onset of transonic escape of hypothetical nitrogen atmospheres from Earth and Mars on ramping up XUV insolation to that experienced in the early pre-main sequence. Given best estimates of lower boundary conditions, we derive how imposing a Knudsen number equal to one at the sonic point specifies a unique polytropic solution to atmospheric escape. The corresponding threshold in XUV flux to drive the transonic outflow defines a conservative regime of applicability for energy-limited parametrization. Our ansatz is predominantly neutral outflow with XUV heating fueling advection. In Sections 4 & 5 we will relax these assumptions.

3.1. Knudsen Onset

A Knudsen number equal to one at the sonic point will specify the escape of a polytropic atmosphere sustainable for an XUV flux that defines an energetic threshold for transonic escape. The Knudsen number (Knudsen 1909) describes the collisionality of a flow, which is calculated for an atmosphere as the ratio of the mean free path to the local scale height of the atmosphere. We derive the scale height using L’hopital’s rule for the sonic velocity gradient (Lamers & Cassinelli 1999), then substitute into the radial derivative of equation (8a), to yield

$$\left[\frac{1}{\rho} \left(\frac{d\rho}{dr} \right)_{sc} \right]^{-1} = - \frac{(1 + \gamma)r_{sc}}{4 + \sqrt{2}\sqrt{5 - 3\gamma}}. \quad (17)$$

The mean free path is the average distance a particle will travel before its next collision. It can be calculated as the reciprocal of the product of the collision cross-section σ_c and the number density up to a factor of order unity. Thus, the Knudsen number in the polytropic model can be expressed as

$$\text{Kn}_{sc} = \frac{4 + \sqrt{2}\sqrt{5 - 3\gamma}}{\sqrt{2}(1 + \gamma)\sigma_c \cdot n(r_{sc}) \cdot r_{sc}} \quad (18)$$

The model exobase separates a collisional thermosphere below ($\text{Kn} < 1$) from the collisionless exosphere above ($\text{Kn} > 1$). We compare our criterion for transonic escape with the numerical and analytic calculations of Johnson et al. (2013a) in Section 3.3. We note that Owen & Jackson (2012) found ballistic escape from some more massive Hot Jupiters on the basis of non-existence of a collisional sonic point but did not explicitly relate this to their polytropic model or XUV flux.

The Knudsen onset for transonic escape should be taken with two caveats:

- I. Collisionality increases with greater ionization due to the greater cross-sections of ion-atom charge exchange and high-frequency atom-electron collisions. To establish a general method to calculate the onset of transonic escape, we choose to work with the neutral onset $\text{Kn}_{sc}^N \sim 1$, using the neutral collision cross-section σ_c^N ; reasonable when advection-dominated and weakly ionized.
- II. In a bulk outflow, the nominal exobase forming before the hypothetical sonic point is consistent with the upper boundary fulfilling the flux constraints of a drifting-Maxwellian Jeans escape (Volkov 2011; Erwin et al. 2013). The energy limit might apply for $\text{Kn}_{sc} \in [1, 3]$, or extend even further (Johnson et al. 2013a), but characterizing the non-linear transition requires both DSMC and hydrocode modeling, so it is beyond the scope of the present study.

Thus, for characterizing rapid mass loss, the neutral onset is highly conservative.

The crux of the polytropic framework is to estimate the threshold XUV flux needed to drive (Eqn 4) transonic hydrodynamic escape for atmospheres of varying gravitational binding and composition. Temperatures and ion production should not be so extreme that line-cooling chokes off the flow, which will be discussed in Section 4. The onset XUV flux is determined by the mass loss rate for the polytropic atmosphere γ_{on} where $\text{Kn}_{sc} = 1$:

$$F_{\text{XUV}}^{\text{on}} = \frac{\Phi_{\text{hyd}}(\gamma_{\text{on}}; \lambda_0, r_0, n_0, \mu, \sigma_c^N) v_{\text{esc},0}^2}{2\pi r_{\text{abs}}^2 \eta_\gamma \eta_{\text{pr}} \eta_c}, \quad (19)$$

mediated by the thermomechanical efficiency η_γ (Eqn 7b), the photoreaction efficiency η_{pr} and the cooling efficiency η_c . The greater collisionality at the sonic point required, the smaller γ_{on} , where the XUV flux rises proportionally with the mass loss rate beyond the onset values.

To find γ as a function of Kn_{sc} , we substitute the sonic-to-base density ratio (Eqn 16b) into Equation (18):

$$\frac{(1+\gamma)(5-3\gamma)\lambda_0}{4(4+\sqrt{2}\sqrt{5-3\gamma})(\gamma-\lambda_0\gamma+\lambda_0)} \cdot \left(\frac{(5-3\gamma)\gamma}{2\gamma+2\lambda_0(1-\gamma)} \right)^{1/(1-\gamma)} - \left(\sqrt{2}\text{Kn}_{sc}\sigma_c n_0 r_0 \right)^{-1} = 0, \quad (20)$$

which defines a dummy function ψ , such that the neutral onset is given by $\gamma_{\text{on}} = \psi(\text{Kn}_{sc} = 1; \lambda_0, r_0, n_0, \sigma_c^N)$. The parameters after the semicolon in ψ are specified as constants for a particular planetary atmosphere in a given regime. We can use the original Bernoulli definition of the exponential $\lim_{j \rightarrow \infty} \left(1 + \frac{x}{j}\right)^j = e^x$, to recover the isothermal limit, of Equation (20) with $j = 1/(1-\gamma)$

$$\lim_{j \rightarrow \infty} \left(\frac{1 + \frac{3}{2j}}{1 + \frac{\lambda_0}{j}} \right)^j \propto \frac{\lambda_0}{6} \cdot e^{3/2-\lambda_0} = \left(\sqrt{2}\text{Kn}_{sc}\sigma_c \cdot n(r_0) \cdot r_0 \right)^{-1}, \quad (21)$$

where the derivation requires Taylor expansion of the denominator. We note that the isothermal solution restricts Kn_{sc} to be specified by the lower boundary conditions. In the polytropic framework, given the best-estimate base density and neutral cross sections, γ_{on} is found implicitly through Equation (20) and selects the contour for the atmospheric structure (Eqn 10). The corresponding flux is given by Equation (19), with a further estimate needed for the absorption radius.

Underlying Equations (19-20) should be approximately consistent local heating rates, especially at the sonic point. Assuming the flow at the sonic point is optically thin to incoming XUV, a physical estimate of XUV heating per unit mass at the sonic point is

$$\overline{q_{sc}} \approx a_\theta \sum_\lambda \eta_{pr}(\lambda) F_{\text{xuv}}(\lambda) \sigma_\lambda / m, \quad (22)$$

where m is the atomic mass, σ_λ and $\eta_{pr}(\lambda)$ are the photoabsorption cross-section and photoreaction efficiency as a function of wavelength (e.g., Huebner & Mukherjee 2015). The prefactor a_θ is equal to unity if consider the heating at the substellar point, or equal to $\cos(66^\circ)$ to account for global averaging of the XUV flux Johnstone et al. (2019). The polytropic model heating per unit mass at the sonic point is given by

$$q_{sc,\gamma} = \left(\frac{\gamma_a}{\gamma_a - 1} + \frac{\gamma}{1 - \gamma} \right) \frac{4 + \sqrt{2}\sqrt{5-3\gamma}}{(1+\gamma) \cdot (1-\gamma)^{-1}} \frac{RT_{sc}u_{sc}}{r_{sc}}, \quad (23)$$

calculated from substituting the sonic density temperature gradient, found by chain rule from Equation (17), into Equation (4). Again, the isothermal limit of $q_{sc} = 3u_{sc}^3/r_{sc}$ can be recovered. The XUV flux found by matching Equation (22) with (23) will not necessarily agree with the onset flux (Eqn 19). There is broad agreement in the cases we explore; however, the atmospheric structure can be useful regardless. We will now discuss the physical inputs for Equation (19).

3.2. Photoevaporation of Nitrogen Thermospheres by Active Stars

Differential rotation in a star's convective envelope generates a magnetic field that confines and heats coronal plasma to millions of kelvin, resulting in XUV emission from metal lines and the free-free continuum. Stars are initially saturated in X-ray emission relative to bolometric luminosity, later losing angular momentum through magnetic breaking of the stellar wind until converging onto a main-sequence activity track for a given mass (Vilhu 1984). Depending on the initial rotation rates of F, G, and K stars, their saturated phase lasts around 10–300 million years, compared to billions of years for the lower mass M-dwarfs due to their persistently long convective turnover timescale (Johnstone et al. 2021).

The evolution of the Sun's XUV flux at 1 AU (Catling & Kasting 2017; Ribas et al. 2005) is given by

$$F_{\text{xuv}}(\tau_{\text{age}}) \approx 23.3 \times 10^{-3} \tau_{\text{age}}^{-1.23} \text{ W m}^{-2}, \quad (24)$$

where τ_{age} is in GYrs, $F_{\text{xuv},\oplus} \approx 4 \times 10^{-3} \text{ W m}^{-2}$. The XUV flux in the Sun's early pre-main-sequence is then $F_{\text{xuv}}(\oplus, 0.1 \text{ Gyr}) \approx 0.4 \text{ W m}^{-2} \approx 100 F_{\text{xuv},\oplus}$, but could have been several times higher if initial rotation was rapid (Johnstone et al. 2021). Variability in the solar cycle leads to a factor of 2 difference between the EUV of the quiet and active Sun (Huebner & Mukherjee 2015). Turning to a $0.09 M_\odot$ M-dwarf, the XUV flux at TRAPPIST-1 b (0.011 AU) during its early pre-main-sequence may have been $\gtrsim 10^4 F_{\text{xuv},\oplus}$ and today it is $\sim 10^3 F_{\text{xuv},\oplus}$ (Fleming et al. 2020). While for the M-dwarf super-Earths LHS-1140 c (0.027 AU) and LHS-

Table 1: Nitrogen Photoabsorption Reactions

Photoreaction	ΔE (eV)	λ_ν (nm)	Excess energy (eV)
$\text{N}_2 + \gamma \rightarrow \text{N}_2^+ + e^-$	15.7	79.2	21.4
$\text{N}_2 + \gamma \rightarrow \text{N} + \text{N}$	12.5	99.2	3.38
$\text{N}_2 + \gamma \rightarrow \text{N}^+ + \text{N} + e^-$	24.4	25.0	32.4
$\text{N} + \gamma \rightarrow \text{N}^+ + e^-$	14.6	85.10	19.0
$\text{N}^+ + \gamma \rightarrow \text{N}^{2+} + e^-$	29.2	42.5	17.3

NOTE— ΔE & λ_ν are the threshold energy and corresponding wavelength of incoming EUV photons for the given pathway. The excess energy of photoreactions in the Modern Solar Spectrum in a period of high activity. Data taken from PHIDRATES database [Huebner & Mukherjee \(2015\)](#).

1140 b (0.09 AU) the XUV fluxes today are approximately $100\times$ and $10 \times F_{\text{XUV},\oplus}$, with b currently in the habitable zone ([Spinelli et al. 2023](#); [Cadieux et al. 2024](#)).

At the base of the thermosphere, photodissociation of dinitrogen produces atomic nitrogen that is advected upwards, while N_2 is replenished from the lower-atmosphere reservoir. For an energy-limited onset we expect that photoionisation of atomic nitrogen is balanced by the advection of ions downstream along a gradient of increasing ionisation fraction. Ion-electron recombination plays a minor role in these conditions (see Sec 4). The flow accelerates sharply, with density dropping to keep mass flux roughly uniform. We expect a relatively sharp N_2/N front followed by an extended N/N^+ front up to the sonic point where, with onset XUV fluxes, the ionisation fraction should remain minor, as is found in [Johnstone et al. \(2019\)](#).

The reaction pathways for XUV absorption are summarized in Table 1, with data from [Huebner & Mukherjee \(2015\)](#). Photodissociation to neutral atoms does not efficiently heat the thermosphere because absorption is constrained by the potential energy of bound states of dinitrogen (e.g., [Heays et al. 2017](#)). To find the global efficiency of heating by photoreactions, when ion-electron recombination and dissociative recombination of nitrogen are low, one can make the approximation that every two atoms lost must have come from a photodissociation event and every ion lost from a photoionisation event. Thus, weighting the average excess energies, the global photoreaction heating efficiency is $\eta_{pr}(f_+^{sc} = 0.1) \approx 1/3$, or $\eta_{pr}(f_+^{sc} = 0.2) \approx 0.45$, where f_+ is the ionization fraction. We note that the efficiency of the *local* heating at the sonic point is determined by excess photoionisation energy only, yielding $\eta_{pr,sc} \approx 0.6$.

Oxygen has a lower dissociation energy than nitrogen, with absorption extending in the UV to ~ 200 nm.

The model of [Johnstone et al. \(2019\)](#) includes UV in their XUV spectrum, tripling the energy available in their $\approx 60F_{\text{XUV},\oplus}^*$. Focusing attention on a pure nitrogen atmosphere allows us to safely neglect detailed photochemistry and means the XUV spectrum mostly overlaps with that driving hydrogen escape. Apart from order unity variation in efficiency, the polytropic heating is agnostic to what composes the XUV spectrum, so fluxes quoted in Wm^{-2} are unaffected. However, the dynamics of oxygen line cooling compared to nitrogen is more heterogenous so we will make direct comparison in Section 4.

The neutral collision cross-section given by $\sigma_c(\text{N} - \text{N}, 10^4 \text{ K}) = 3.9 \times 10^{-20} \text{ m}^2$ ([Kislyakova et al. 2019](#)). Charge-exchange is effective enough that even for a weakly ionised plasma, it could more than double the total cross-section: $\sigma_c(\text{N} - \text{N}^+, 10^4 \text{ K}) = 5 \times 10^{-19} \text{ m}^2$ ([Laricchiuta et al. 2009](#)). The electron-neutral cross section can be found somewhere inbetween $\sigma_c(\text{N} - e^-, 10^4 \text{ K}) = 2 \times 10^{-19} \text{ m}^2$. For a species mixture, an effective collision cross-section against the bulk density can be considered:

$$\sigma_c = \sum_k \frac{n_k \sigma_{k,c}}{n}. \quad (25)$$

Considering an ionisation fraction ~ 0.1 we find $\sigma_c(\text{N} - \text{all}, 10^4 \text{ K}) = 1.1 \times 10^{-19} \text{ m}^2 \sim 3 \times \sigma_c^{\text{N}}$.

3.2.1. Young Sun Earth

This section presents a model of evaporation of Earth's atmosphere prescribed to be pure nitrogen in the raised XUV output of the Young Sun. Though the Early Earth is thought to have had a CO_2 -rich atmosphere (e.g., [Lammer et al. 2018](#)), nitrogen's role in habitability makes this an interesting exo-Earth scenario. Somewhat coincidentally, the [Johnstone et al. \(2019\)](#)

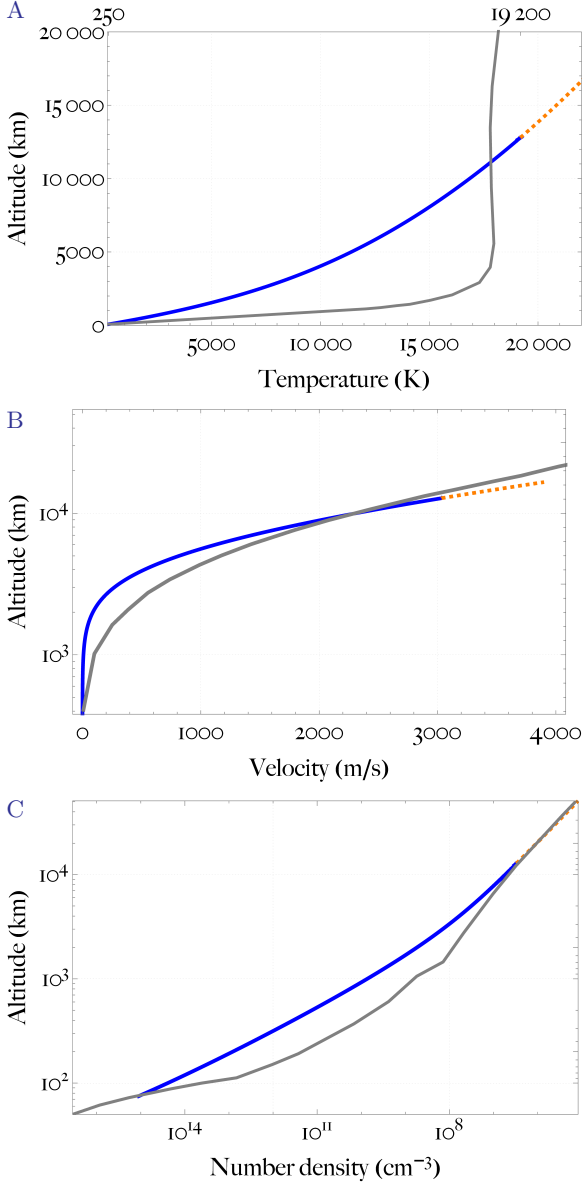


Figure 4: The polytropic onset solution $(\lambda_0, \gamma_{\text{on}}) = (358.4, 0.78)$ for the temperature, velocity and number density profiles (blue) for an Earth-like planet hosting a pure nitrogen thermosphere. The dashed-orange line begins at the sonic level $r_{sc} \approx 3R_{\oplus}$. The hydrocode profiles from [Johnstone et al. \(2019\)](#) are presented for comparison in grey. The XUV flux required to drive the transonic hydrodynamic escape is estimated $F_{\text{XUV}}^{\text{on}}(\text{YSE}) \approx 0.8 \text{ W m}^{-2}$, or equivalently, $\gtrsim 200F_{\text{XUV},\oplus}$.

hydrodynamic simulations of Young Sun Earth escape turn out to be close to the neutral onset that we here derive from the polytropic framework, offering the opportunity for intercomparison. Though we note that the collisional onset within the hydrocode model could be different, depending on choice of parameters.

The lower boundary is set to a mesopause-like altitude of 75 km with an inventory of 10^{15} cm^{-3} nitrogen atoms and a temperature of 250 K, yielding $\lambda_0 = 358.4$ noting $M_{\oplus} = 5.97 \times 10^{24} \text{ kg}$ and $R_{\oplus} = 6.378 \times 10^6 \text{ m}$ (equatorial). Calculated with Equation (20), the neutral onset $\gamma_{\text{on}} = 0.78$ provides enough implicit heating for the scale height to develop such that the outflow remains collisional out to the sonic point. This corresponds to almost 9 orders of magnitude change in number density from the base to the sonic radius (Fig 4). The sonic radius is calculated as $3 \times$ the planetary radius (Eqn 13), or at an altitude of approximately 12 800 km. The temperature monotonically increases to 19 200 K at the sonic radius, yielding a sonic-to-base temperature ratio of $77 \times$ (16a). The velocity is inappreciable until a couple of thousand kilometres in altitude before rising steeply to the sonic speed at 3 km s^{-1} — the total change in Mach number is seven orders of magnitude. Past the sonic radius, a dashed line shows a continuation of the polytropic solution for each profile in Figure 4. However, the behaviour and forcing downstream of the sonic point do not affect the mass loss rate or the atmospheric structure upstream.

The polytropic model for Young-Sun Earth onset (Eqns 15 & 20) yields a mass loss rate of $1 \times 10^9 \text{ g s}^{-1}$ or $4 \times 10^{31} \text{ atoms/s}$. Based on this rate, six bars of an N_2 atmosphere could be lost in a million years. As noted by [Johnstone et al. \(2019\)](#), the discussion of fluxes is always up to an order unity factor as studies use different averaging conventions and a range of spectral models. The flux-receiving cross-section has a larger area than the projected surface of the planet (πR_{pl}^2) — larger due to heating being significant out to a few planetary radii. We approximate the geometric factor $R_{abs} = \sqrt{2}R_{pl}$ (Eqn 6) following [Catling & Kasting \(2017\)](#). We also account for the thermomechanical efficiency of the hydrodynamic expansion $\eta_{0.78} \approx 0.83$ and the efficiency of heating via photoelectrons $\eta_{pr} \approx 1/3$. Altogether, we find the flux incident on the sub-stellar column needed to trigger the onset of transonic hydrodynamic escape (Eqn 19) to be $F_{\text{XUV}}^{\text{on}}(\text{YSE}) \approx 0.8 \text{ W m}^{-2}$, equivalent to $\gtrsim 200F_{\text{XUV},\oplus}$. However, a subsonic onset of bulk outflow may be possible fluxes for an order of magnitude lower $\sim 20F_{\text{XUV},\oplus}$. Accounting for the uncertainty in the initial rotation rate of the Sun ([Johnstone et al. 2021](#)) and neglecting non-LTE cooling for now, the transonic escape of a thick secondary atmosphere during the saturated phase is plausible.

The $\gamma_{\text{on}} = 0.78$ mass loss rate happens to be $1/2 \times$ the rate in [Johnstone et al. \(2019\)](#), so broadly similar profiles might be expected. Figure 4 displays the curves calculated with Kompot from [Johnstone et al.](#)

(2019) for comparison. The temperature-profile comparison highlights how the single polytropic index γ cannot account for the differential steepness in the middle and upper atmospheres. However, despite that dissimilarity, the temperatures at the polytropic sonic radius agree to within 10%. The density profile from Figure 4 carries the dissimilarity in temperature to differing scale heights. However, the steeper-then-flatter pattern converges to a similar density where the polytropic atmosphere goes sonic to within a factor of two. The velocity profiles are similar, though the hydrocode-calculated acceleration ramps up more quickly. The broad agreement at the sonic point with Johnstone et al. (2019) indicate that the polytropic framework gives plausible results. Such results would not have been independently forthcoming from the energy-limited parametrization or from an isothermal Parker wind model.

3.2.2. Young Sun Mars

Following the last section, we now present a model of evaporation of a nitrogen from Mars in the raised XUV output of the Young Sun. Early Mars may have had more than 0.1 bars of nitrogen (Hu & Thomas 2022). However, our primary motivation is to gain insight into exo-Mars planets and the landscape of high molecular weight escape. Follow-up work of coupling the polytropic model to a chemical kinetics code with a CO₂ photochemistry network is in progress (Blumenthal et al., in prep).

For a base temperature 200 K, noting $M = 6.39 \times 10^{23}$ kg and $R = 3.39 \times 10^6$ m (equatorial), the escape parameter for Mars is $\lambda_0 = 105$. For a base inventory of 10^{14} cm⁻³ nitrogen atoms, Equation (20) yields $\gamma_{\text{on}} = 0.826$. Reducing the base temperature from 200 K to 150 K increases $\lambda_0 = 140$ and a steeper inversion of $\gamma_{\text{on}} = 0.80$ is required to remain collisional out to the sonic point. On the other hand, increasing the base density to 10^{15} cm⁻³ allows a less steep inversion of $\gamma_{\text{on}} = 0.86$. For $\gamma_{\text{on}} = 0.826$, the sonic radius is $3.5\times$ the planetary radius or at an altitude of approximately 8500 km (Fig 5). The temperature monotonically increases to 3600 K at the sonic radius, yielding a sonic-to-base temperature ratio of $18\times$.

The indicative Young-Sun Mars transonic onset (Eqn 19) yields a mass loss rate of 3×10^8 g s⁻¹ or 1.3×10^{31} atoms per second or 20 bars of N₂ per million years. Using the same efficiency factors as from the Earth model, the flux incident on the sub-stellar column $F_{\text{XUV}}^{\text{on}}(\text{YSE}) \approx 0.2$ W m⁻², equivalent to $\gtrsim 50 F_{\text{XUV},\oplus}$ or $100\times$ Modern Day Mars XUV. The sonic temperatures in the $\gamma_{\text{on}} = 0.80$ and $\gamma_{\text{on}} = 0.86$ cases are 3100 K and 4200 K, respectively. The resultant difference in mass loss is less

than 10 % due to the square-root dependence of the sonic velocity on temperature. This relative insensitivity to the lower boundary conditions highlights the better physical accuracy of the polytropic model compared to the isothermal Parker wind.

Tian et al. (2009) found hydrostatic instability and rapid escape of a CO₂ atmosphere on Early Mars for $\sim 20\times$ Modern Day Mars XUV. However, this is not inconsistent with the higher XUV required for transonic onset reported here because subsonic outflow could be driven at those lower fluxes. In conclusion, the hypothetical transonic loss of a nitrogen atmosphere from Mars in the saturated phase of the Young Sun would have been possible. Furthermore, the atmosphere of an Exo-Mars in the Habitable Zone of an M dwarf would not survive on geological timescales.

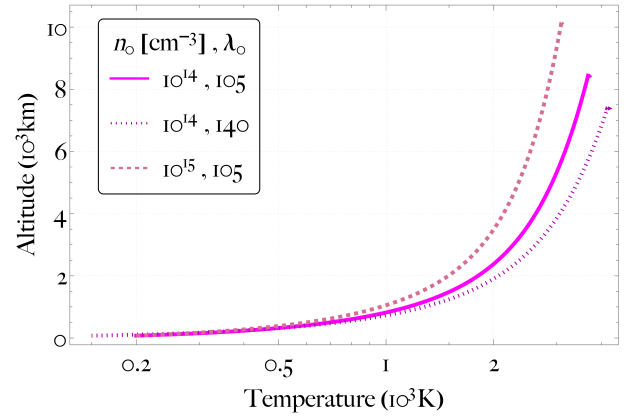


Figure 5: Temperature profiles for hypothetical nitrogen escape from Young-Sun Mars ($T_0, n_0, \lambda_0, \gamma_{\text{on}}$) = (200 K, 10^{14} cm⁻³, 105, 0.826) (solid), (150 K, 10^{14} cm⁻³, 140, 0.8) (dashed), (200 K, 10^{15} cm⁻³, 105, 0.86) (dotted).

3.3. Comparison with Johnson et al. (2013a,b)

The analytic transonic criterion of Johnson et al. (2013a) was employed by Gronoff et al. (2020) to evaluate the propensity for atmospheric escape across a survey of planets. Notably, the Direct simulation Monte Carlo models from Johnson et al. (2013a) suggest that the energy-limited mass loss rate applies well at onset and for a range of subsonic flow at smaller XUV fluxes. However, (Johnson et al. 2013a) explore a limited set of assumptions and regimes, so determining the general extent to which the energy limit remains valid before transitioning non-linearly to a roughly Jeans-type escape remains a key unresolved question in the field. On comparing Equation (19) with "Equation (10)" from Johnson et al. (2013a), we see that each calculation estimates the total net heating required to drive transonic

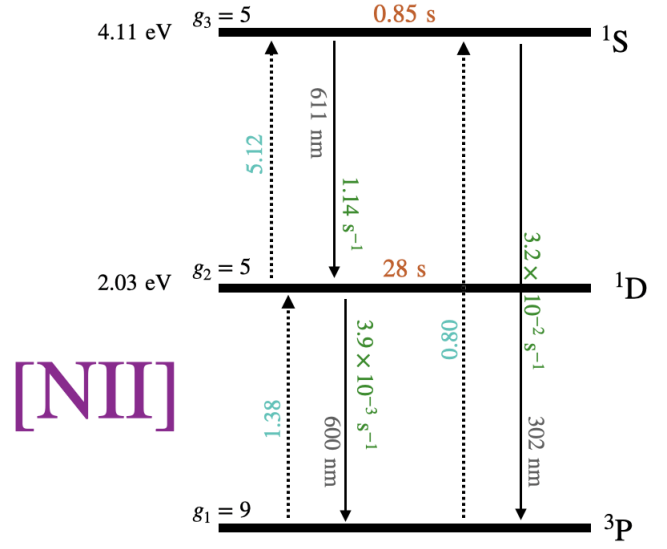
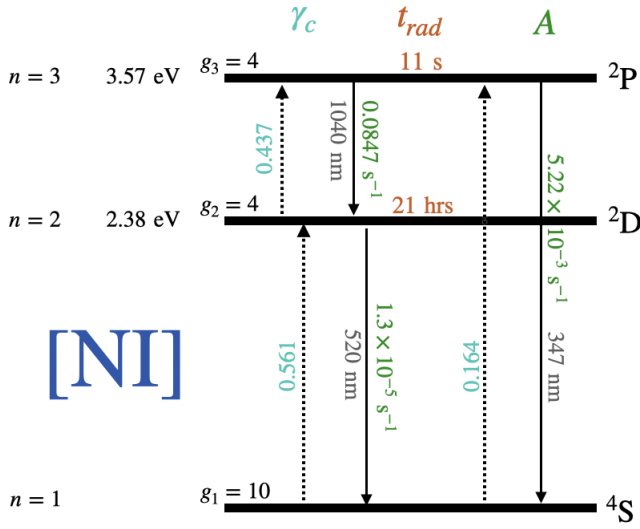


Figure 6: Grotrian level diagram for the first three levels of neutral and singly ionised nitrogen. The coefficients for the collisional excitation γ_c , the radiative lifetime of the level t_{rad} and the transition Einstein-A from Nakayama et al. (2022) are displayed.

outflow at an order-unity Knudsen number at the sonic point. For Young-Sun Earth, Johnson et al. (2013a,b) identify the transonic onset at $\gtrsim 100F_{\text{XUV},\oplus}$, consistent with our results. The polytropic model presented here further enables analytic determination of the sonic scale height and velocity, as well as evaluation of the thermomechanical and line cooling efficiency from the atmospheric structure. We also incorporate a critical estimate for the photoreaction efficiency factor of a nitrogen atmosphere (see Table 1). In subsequent sections, we refine the transonic criterion by analyzing the breakdown of neutral Knudsen-onset assumptions and mapping the landscape of high molecular weight escape (see Fig 11).

4. ACCOUNTING FOR NON-LTE COOLING

The previous section discussed the conditions required for the transonic escape of secondary atmospheres for Mars-to-Earth-sized planets while neglecting the effects of forbidden line cooling. We will now test the primacy of atomic line cooling in the evolution of secondary atmospheres found by Nakayama et al. (2022), but for the hydrodynamic rather than hydrostatic regime. We introduce the simplifying approximation of a three-level model of electron-impact excitation of forbidden lines that cool directly to space. The non-LTE radiative transfer of molecular lines, shown to be important in escaping steam atmospheres (García Muñoz et al. 2024), is not discussed here.

4.1. Three-level Model for Electron Excitation of Atomic Lines

The polytropic framework admits atomic and molecular cooling estimates diagnosed from the atmospheric structure. For a polytropic solution to represent a consistent, steady state, the line cooling rate per unit mass should be lower than the polytropic heating throughout the extent of the atmosphere. The total line cooling luminosity informs the efficiency factor for the energy limit. Collisions between atoms, molecules, electrons, and ions excite vibrational, rotational modes, and electronic states, which can be relaxed by further collisions or by spontaneous emission of light. Electronic states are available to ambient temperatures of 0.1 eV to 1 eV, equivalent to 10^3 K to 10^4 K , or greater. In Local Thermodynamic Equilibrium (LTE), the photons are honorary gas particles, meaning that the local emission per unit mass depends only on a single temperature field and is independent of local densities. Maintained by collisions, the well-known Boltzmann formula gives the population ratio between levels j and i : $\frac{n_j}{n_i} = \frac{g_i}{g_j} \exp\{-E_{ji}/k_B T\}$, where E_{ji} is the excitation energy, g_i, g_j are the level density of states and k_B is the Boltzmann constant (e.g., Feynman et al. 2011). The resulting volumetric cooling rate from some level j to a lower level i via spontaneous emission is given by $Q_{ji} = \frac{n_i g_i}{g_j} \exp\{-E_{ji}/k_B T\} A_{ji} E_{ji}$. Collisions with electrons dominate excitations. For example, in the case of nitrogen, the electron-ion collision frequency ν_{e-i} is approximately $160\times$ that for ion-ion; $\nu_{e-i} \sim \sqrt{m_i/m_e} \nu_{i-i}$, where m_i, m_e are the ion and electron masses.

The other density regime is the coronal limit, where collisional excitations are in dynamic balance with spontaneous emission - a simple non-LTE limit. The volu-

metric cooling rate then becomes independent of A_{ul} in the two-level atom approximation: every electron excited to the upper level spontaneously decays, so that

$$Q_{ul}^{(2)} = n_l C_{lu} E_{ul}, \quad (26a)$$

$$C_{lu} = \gamma_c n_e \frac{8.629 \times 10^{-6}}{g_l \sqrt{T}} \exp\left(-\frac{E_{lu}}{k_B T}\right), \quad (26b)$$

where C_{lu} is collisional excitation coefficient from the lower l to upper level u and γ_c the effective collision strength; the formula takes takes number densities in cm^3 and temperatures in K (Nakayama et al. 2022). An important note is that the two-level coronal cooling scales as the density squared $\propto n_l n_e$. The two-level critical density $n_{cr}^{(2)}$ separating the LTE and coronal regimes is given by

$$n_{cr}^{(2)} = \frac{A_{ul}}{C_{ul}}, \quad (27)$$

where the collisional deexcitation coefficient is

$$C_{ul} = \gamma_c n_e \frac{8.629 \times 10^{-6}}{g_u \sqrt{T}}, \quad (28)$$

and if $n_e \ll n_{cr}^{(2)}$ the plasma will be in the coronal regime.

In this sub-section, we'll explore in detail the states of the neutral nitrogen atom (NI) described by three quantum numbers: principal, orbital angular momentum and intrinsic angular momentum. This accounts for interparticle electrostatics through spin-spin and orbit-orbit coupling but neglects spin-orbit coupling and the associated fine structure. The first three levels of NI are displayed in Figure 6 adopting term notation, along with those of NII. All data are taken from Nakayama et al. (2022), including those of the oxygen lines in OI and OII, which we will sometimes reference for comparison.

The longest wavelength electric-dipole-allowed transition to ground is a strong line called the resonance line. The NI resonance line is $^4P \rightarrow ^4S$ with $E_{41} = 10.3 \text{ eV}$, $\lambda_\nu^0 = 120 \text{ nm}$ and a radiative lifetime of just 3 ns. However, terrestrial upper atmospheres rank, in terms of astrophysical line sources, as warm $\sim 10^4 \text{ K}$ and tenuous $n_e \ll 10^{10} \text{ cm}^{-3}$, so the resonance line is dramatically underactivated compared to when in hot and dense conditions that make up LTE. So the low-lying electric-dipole-forbidden transitions, which are show in Figure 6, dominate. At temperatures up to 20 000 K, a three-level atom is sufficient to model the collisional-radiative non-equilibrium explicitly. The first two excited states have long radiative lifetimes, but in the three-level coronal limit, the cooling contribution is only weakly dependent on the Einstein-A.

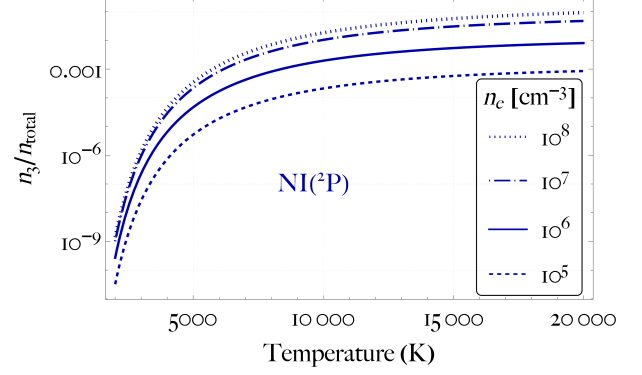


Figure 7: The ratio of nitrogen atoms excited two levels above ground n_3 to the total population n_{total} plotted as a function of temperature and electron density; calculated with a three-level atom approximation (Eqn 29). Note that the cooling luminosity in each line is directly proportional to the number of atoms in each excited level.

So we can approximately model [NI] as a three-level atom excited by electron impact, as has been done for fine structure of the NII ground state by Goldsmith et al. (2015). The populations of these three levels depend on the collisional and radiative Einstein coefficients such that

$$\begin{aligned} -(A_{32} + C_{32} + C_{31})n_3 + C_{23}n_2 + C_{13}n_1 &= 0 \\ (A_{32} + C_{32})n_3 - (A_{21} + C_{21} + C_{23})n_2 + C_{12}n_1 &= 0 \\ C_{31}n_3 + (A_{21} + C_{21})n_2 - (C_{12} + C_{13})n_1 &= 0 \\ n_3 + n_2 + n_1 &= n_{total} \end{aligned} \quad (29)$$

Reduction of these equations to the population ratios yields a dependence only on the electron density and temperature as displayed in Figure 7. The three-level critical densities differ from the two-level model. The population of the third level only begins to be independent of density around $n_3^{cr} \sim 10^8 \text{ cm}^{-3}$, which is about an order of magnitude greater than that found with the inadequate two-level model. We have neglected photochemical production of excited states which should be reasonable for nitrogen atmospheres but might be major in a carbon dioxide atmosphere.

Exploring [NI] in Figure 6, the long radiative lifetime of the first excited level at 2.4 eV above ground (indexed 2) of NI at 21 hours means that the $2(^2D) \rightarrow 1(^4S)$ ‘nebular’ forbidden transition is a poor cooling mechanism. The second excited level, or third level of the atom, contributes two lines at $E_{31} = 3.6 \text{ eV}$: the ‘transauroral’ transition $3(^2P) \rightarrow 1(^4S)$ has transition rate $A_{31} = 5.22 \times 10^{-3} \text{ s}^{-1}$, which is minor compared to the $3(^2P) \rightarrow 2(^2D)$ ‘auroral’ transition with $A_{32} =$

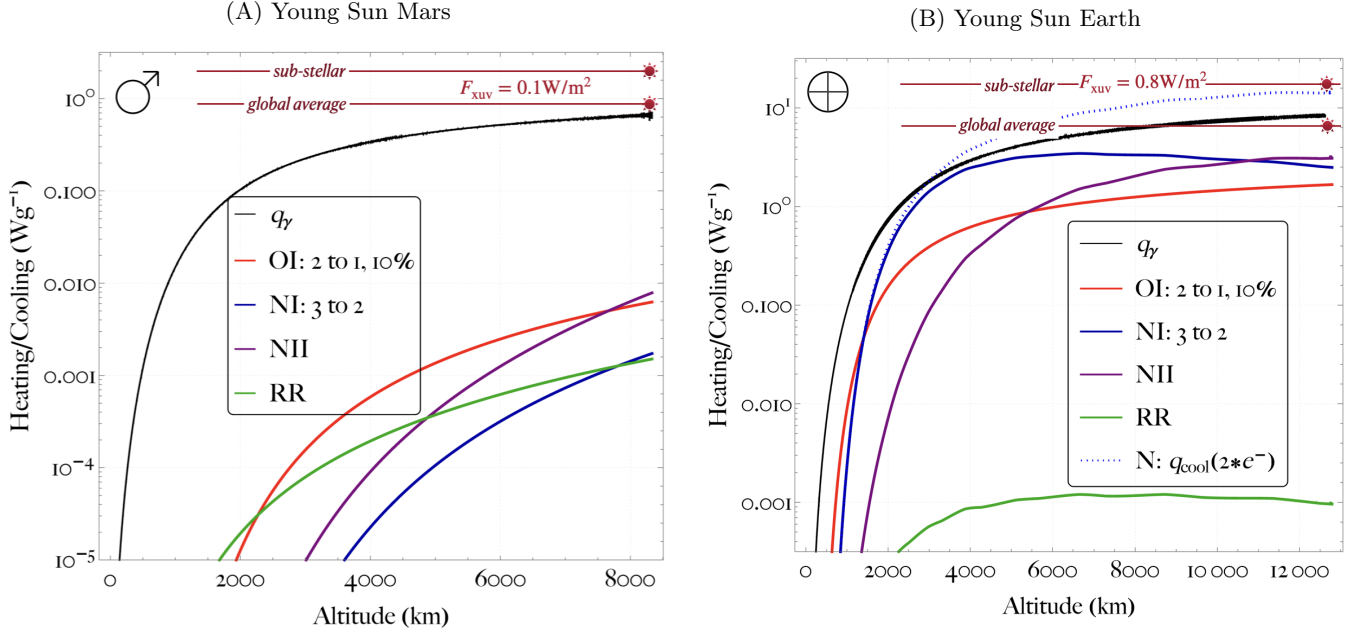


Figure 8: Polytropic heating (q_γ in black; see Eqn 4) compared to forbidden line cooling (blue, red and purple; see Eqn 29) and recombination cooling (green) per unit mass. Displayed optically thin heating expected from the incoming sub-stellar and globally averaged XUV flux of (see Eqn 22). In blue is the cooling from the auroral transition of NI and in red is the cooling effect of mixing in 10% oxygen, which is dominated by the nebular transition. Lastly, in green is the cooling from radiative recombination of N^+ . (A) Young Sun Mars ($n_0, \lambda_0, \gamma_{\text{on}} = (10^{14} \text{ cm}^{-3}, 105, 0.826)$). Cooling is calculated by assuming an upper-bound uniform free electron density of 10^6 cm^{-3} and corresponding density of N^+ (NII) by quasineutrality. (B) Cooling for the Young Sun Earth hydrodynamic onset is calculated using electron profile from Johnstone et al. (2019), which peaks at $10^{6.5}$ electrons cm^{-3} . The effect of doubling the estimated electron densities on the total line cooling from nitrogen is shown in dashed-blue ($q_{\text{cool}}(2 \times e^-)$).

$8.47 \times 10^{-2} \text{ s}^{-1}$. Thus, the third excited level has a lifetime of 12 s and cooling is dominated from the first three levels by $[\text{NI}]_{1.04\mu\text{m}}^{3 \rightarrow 2}$ with $E_{32} = 1.2 \text{ eV}$.

We use a cool-to-space approximation as the forbidden lines make up a small optical depth due to their small Einstein-A (López-Puertas & Taylor 2001). We calculate the optical depth assuming Doppler broadening only:

$$\tau_{\nu_{ul}} = \left(\frac{hc_l}{E_{ul}} \right)^3 \frac{\sqrt{\gamma} g_u N}{8\pi^{3/2} g_l} \frac{A_{ul}}{c_\gamma}, \quad (30)$$

where N is the total column density above the thermobase, h Planck's constant and c_l the speed of light (Kunc & Soon 1989). The escape probability formulation used in Nakayama et al. (2022) is not necessary for this regime as line photons propagated below the thermobase are lost as blackbody radiation - still contributing a net cooling to the thermosphere.

4.2. Is Line cooling Minor in the Weakly Ionised Onset of Hydrodynamic Escape?

4.2.1. Young Sun Mars

The heating at the sonic point in the polytropic onset model for Young Sun Mars ($10^{14} \text{ cm}^{-3}, 105, 0.826$) is consistent to within a factor of two of the optically thin heating expected from the incoming globally averaged XUV flux of 0.1 W m^{-2} (see Eqns 23-22). Figure 8A shows how in an advection-dominated nitrogen flow at these temperatures, atomic line cooling is not significant compared to the heating required for model Knudsen onset. We assume an upper-bound uniform free electron density of 10^6 cm^{-3} . NI is inefficient at cooling compared to CI and OI at these temperatures. For example, the Einstein coefficient for the $2 \rightarrow 1$ transition is approximately $700\times$ larger for OI than NI, explaining how a 10% mixing ratio of oxygen would dominate the cooling. However, the model heating is more than $10\times$ the OI cooling, so we would still expect consistent onset hydrodynamic escape even for a pure oxygen thermosphere. Radiative recombination (see Section 5) contributes the greatest cooling below 2000 km. Mars, with a gravitational binding atmosphere a fifth of Earth's, thus represents well the limit where line cooling is not

the controlling factor in the retention of a secondary atmosphere.

4.2.2. Young Sun Earth

The Knudsen-onset from the polytropic model for a nitrogen-dominated atmosphere (10^{15} cm^{-3} , 358.4, 0.78) is again within a factor of two of the optically thin heating expected from the incoming globally averaged XUV flux of 0.8 W m^{-2} found to be required in Section 3.2.1. However, compared to Mars, the hotter aeronomy required to escape Earth's gravitational well results in significant line cooling. The electron density profile used for all the curves is from [Johnstone et al. \(2019\)](#), where we also double the electron density in the profile as a sensitivity test. The profile has a peak electron density of $3 \times 10^6 \text{ cm}^{-3}$, above which the density decreases towards the sonic point and beyond.

The contributions to cooling are as follows. The blue curves in Figure 8B show cooling from the auroral transition of neutral nitrogen. In addition, the cooling effect from mixing in 10% atomic oxygen is shown through the dominant nebular transition of OI in red. Figure 8B shows how cooling is minor at the sonic point compared to the XUV heating. The auroral cooling of NI at 1040 nm in blue almost matches the implicit heating in the middle atmosphere. The NII cooling assumes nitrogen ion density equal to the electron density by quasineutrality. Due to shorter radiative lifetimes (see Fig 6), the line cooling of NII becomes dominant at the sonic point despite being a minor fraction. The OI nebular line dominates at the bottom of the atmosphere, where temperatures are low. Radiative recombination of atomic ions and electrons is minor in the upper atmosphere.

Though the cooling integrated over the model atmosphere is minor, the comparable heating and cooling in the middle atmosphere leads us to set the efficiency factor from cooling as $\eta_c = 0.5$. An XUV flux twice as intense, corresponding to $\sim 400 F_{\text{XUV},\oplus}$, is then required to account for non-LTE cooling. When the ionization fraction is doubled compared to [Johnstone et al. \(2019\)](#) the total nitrogen cooling dominates over the $\sim 200 F_{\text{XUV},\oplus}$ polytropic heating in the atmosphere above 3000 km (Fig 8B). To explore these sensitivities, we will next explore the dynamics of hydrodynamic escape and hydrostatic instability with freely varying electron densities in an analytic model of the collisional-radiative thermostat.

5. COLLISIONAL-RADIATIVE THERMOSTAT AND GLOBAL ION OUTFLOW

We now focus our attention towards the dynamics of predominantly ionized outflow. We show that the large escape velocity of super-Earths means that an XUV-driven global ion outflow is the only route towards rapid escape of a secondary atmosphere. The formulation of ion-electron effects in the instability of forced hydrostatic atmospheres is also key to understanding the differing conclusion of the present study to that of [Nakayama et al. \(2022\)](#).

5.1. Plasma Escape Temperature

Higher ionization fractions lead to greater line cooling, reducing the tendency of an atmosphere to escape. The counter-effect, hitherto unremarked upon in the context of global loss of secondary atmospheres, is the increase in sound speed in an ionized atmosphere, or equivalently, the reduction in effective mean molecular weight, and thus a reduced escape temperature via $GM\mu/(k_B T_{\text{esc}} r) = 2$ (see Eqn 12). An ambipolar electrostatic field couples the plasma, reducing escape of electrons and promoting escape of ions (e.g., [Bauer & Lammer 2004](#); [Koskinen et al. 2013](#)).

The ion-acoustic speed of sound for a quasineutral mixture without secondary ionization is

$$c_{i-a}^2 = \frac{\gamma_e f_+ k_B T_e + \gamma_i f_+ k_B T_i + (1 - f_+) \gamma_n k_B T_n}{f_+ m_e + f_+ m_i + (1 - f_+) m_n}, \quad (31)$$

where f_+ is the ionization fraction, and m_e, m_i and m_n refer to the electron, ion and neutral atom masses respectively (e.g., [Chen 2016](#)). We can assume ion-electron thermalization and approximately isothermal outflow in these high XUV flux conditions, such that neutral, ion and electron temperatures and ratios of specific heat are equal $T_i \approx T_e, \gamma_i = \gamma_e = 1$. The ion-acoustic sound speed can then be simplified to

$$c_{i-a}^2 \approx \frac{(1 + f_+) k_B T_i}{m_i}. \quad (32)$$

Thus, the mean molecular weight will be given by

$$\mu(f_+) \approx \frac{m_i}{1 + f_+}, \quad (33)$$

so for $f_+ = 0.5$ or 1, the mean molecular weight is 2/3 or 1/2 the neutral equivalent. We define the local *plasma* escape temperature as the escape temperature when the local ionization fraction is roughly unity:

$$T_{\text{esc}}(f_+ = 1) = \frac{m_i}{2} \frac{v_{\text{esc}}(r)^2}{4k_B} = \frac{T_{\text{esc}}(f_+ = 0)}{2}. \quad (34)$$

As displayed in Figure 10, the escape temperature for neutral outflow from Earth is approximately 18 000 K

but for a fully ionized atmosphere only 9000 K. This simple derivation captures the principal physics, but ionospheric processes are highly non-linear and this effect could be also enhanced (Collinson et al. 2024). Rocky exoplanet ionospheres are ripe for research.

5.2. Ion-Electron Recombination

In the lower and upper layers of Earth’s ionosphere, the primary sinks of photoelectrons are dissociative recombination of molecular ions and ambipolar diffusion, respectively (Bauer & Lammer 2004). These mechanisms require a background of molecular and neutral species, which close the chemical network via charge transfer. The radiative recombination of ions and electrons, though significant in the F2 layer, remains minor throughout the atmosphere (Solomon 2010). However, under the raised XUV fluxes that yield extended ionospheres and greater total electron content, radiative recombination can become the primary sink for photoelectrons (e.g., Nakayama et al. 2022).

To introduce the role of recombination, we first compare the dynamics of radiative-recombination cooling with atomic-line cooling. The rate of dielectronic recombination, which proceeds via a metastable intermediate, was calculated with a fit from Zatsarinny et al. (2004, 2005) and found to be minor for $200 \text{ K} < T < 20\,000 \text{ K}$, only equalling the radiative recombination rate at $\approx 27\,000 \text{ K}$. Hence, dielectronic recombination is negligible for the conditions considered in this study. The derivation of radiative recombination (RR) rates takes advantage of photoionization cross-section data, being the time-reversed processes, and is fit with the following formula from Badnell (2006):

$$\alpha_{\text{RR}}(T) = A \left[\sqrt{T/T_0} \left(1 + \sqrt{T/T_0} \right)^{1-B-C \exp(-T/T_2)} + \left(1 + \sqrt{T/T_1} \right)^{1-B-C \exp(-T/T_2)} \right]^{-1}, \quad (35)$$

where $(T_0, T_1, T_2, A, B, C) = (9.467 \times 10^{-2} \text{ K}, 2.954 \times 10^6 \text{ K}, 6.379 \times 10^4 \text{ K}, 6.387 \times 10^{-10} \text{ cm}^3 \text{ s}^{-1}, 0.7308, 0.2440)$. The timescale of thermalization via collisions t_{th} remains shorter than the recombination timescale t_{RR} even when the photoionization rate $1/t_{pi}$ is fast, $t_{th} \ll t_{RR} \sim t_{pi}$, meaning that for each creation of a photoelectron, a thermal electron and an ion recombine. The average photon energy from recombination to N is $\sim h\nu_1 + 3k_B T_e/2$, but the thermal loss from the electron gas is only the continuum part $\sim 3k_B T_e/2$. The difference in radiative recombination between its total and cooling luminosity is that the potential energy of the atom gained by ionization is never transferred to

the electron gas. Accordingly, the ionization potential is considered as an inefficiency of photoionization heating $\eta_{pi} \approx 1 - \nu_1/\bar{\nu}$ throughout our calculations. An exact formula for recombination cooling can be found in Tucker & Gould (1966).

We compare the ratio of the volumetric line cooling to RR cooling in Figure 9 for varying ionization fractions f_+ . Recombination is dominant by several orders of magnitude at $\sim 10^3 \text{ K}$, with excitation of atomic lines increasing steeply with temperature until matching recombination at $\sim 3000 \text{ K}$ and going on to dominate by up to several orders of magnitude at 10^4 K . Nakayama et al. (2022) calculate radiative recombination via an unspecified prescription and do not discuss its dynamics in detail, so direct comparison is unavailable. However, their conclusion that the key role of forbidden-line cooling in escape is not superseded by recombination cooling agrees with the work reported here.

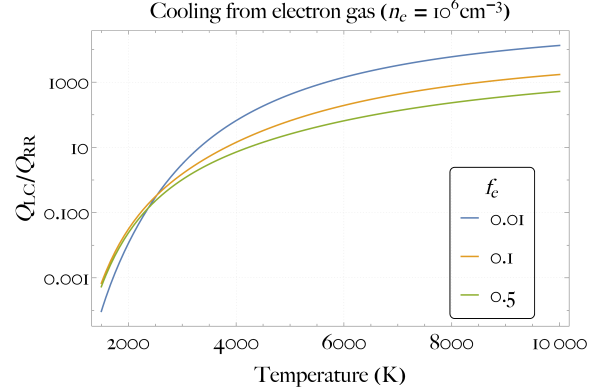


Figure 9: Ratio of local cooling luminosities from excitation of atomic lines Q_{LC} and ion-electron radiative recombination Q_{RC} . The electron density is 10^6 cm^{-3} . The density of neutral nitrogen atoms is varied from 10^8 cm^{-3} (blue) and 10^7 cm^{-3} (orange) and 10^6 cm^{-3} (green) at temperatures from 1500 K to 10 000 K. This is roughly equivalent to ionisation fractions of $f_+ = 0.01, 0.1, 0.5$.

5.3. The Thermostat of Photoionisation versus Line Cooling

In this sub-section, we explore how photoionization both heats the atmosphere but also generates free electrons that excite greater line cooling. We consider quasineutral nitrogen layers in the upper atmosphere that are optically thin to incoming XUV photons. The rate ions are advected away, through either acceleration in bulk outflow or molecular diffusion, can be included

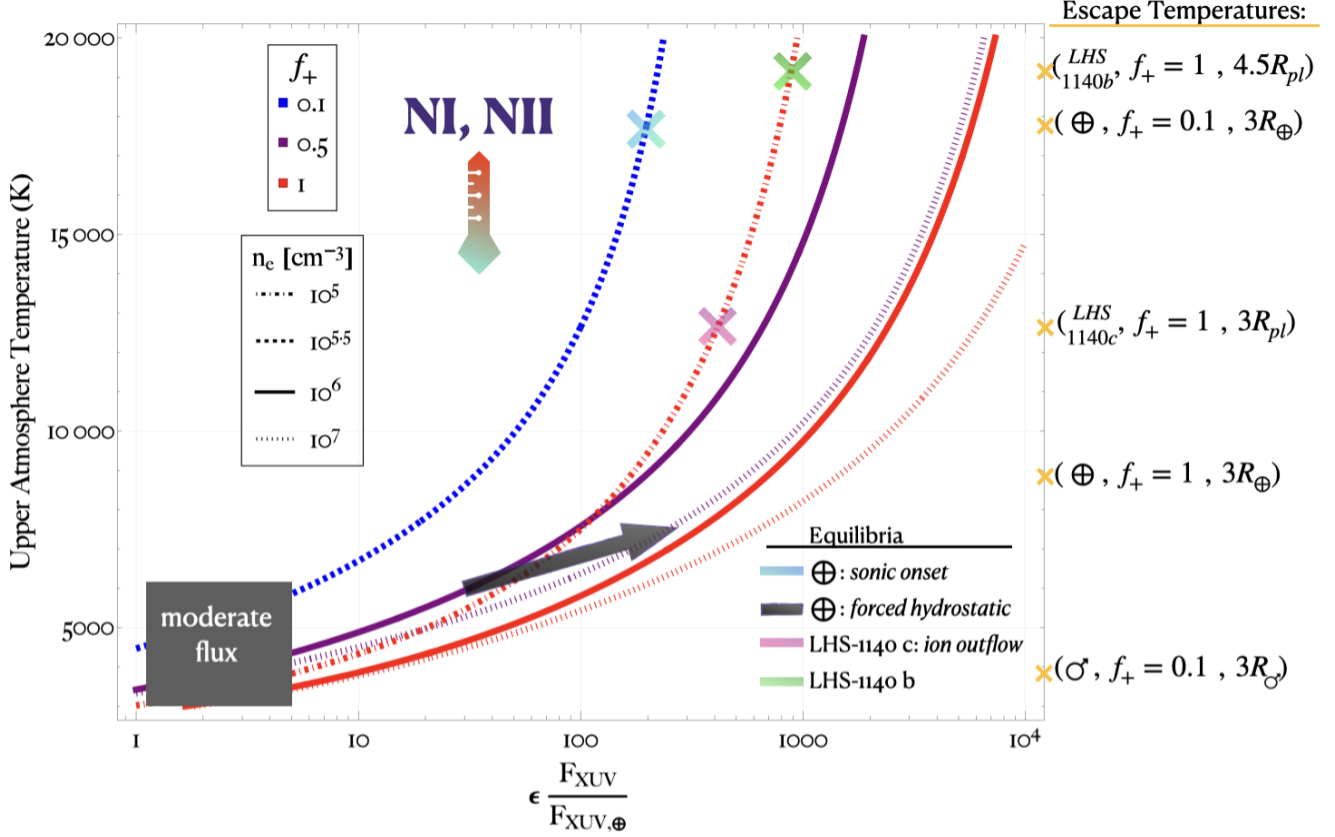


Figure 10: The upper atmosphere temperatures determined locally by the collisional-radiative thermostat as a function of XUV flux relative to Modern Solar conditions and electron densities. The escape temperatures are shown for each planet with a range of ionisation fractions f_+ (Eqns 12 & 33). *Note for interpretation that a hydrostatic exobase at greater than half the escape temperature is unstable and the sonic point of a hydrodynamic outflow will approximately reach the escape temperature.* A range of ionisation fractions 0.1 – 1 and local electron densities $10^5 - 10^7 \text{ cm}^{-3}$ are shown identified by legends on the lefthand side. Advection reduces the energy available from XUV heating, along with thermal conduction and the assumed minor optical attenuation; expressed in the prefactor ϵ . The blue cross highlights a local equilibrium at the sonic point roughly consistent with the Young Sun Earth polytropic onset at $\approx 400 F_{\text{XUV},\oplus}$ (see Section 3.2.1). The evolution in the black arrow illustrates a feedback between photoionisation and line cooling on temperature relevant to Nakayama et al. (2022). However, if the hydrostatic Earth-like atmosphere reaches high ionization fractions in the black-arrow evolution it becomes unstable to escape. The pink and green crosses indicate the XUV fluxes required to drive global ion outflow from LHS-1140 c and LHS-1140 b based on their plasma escape temperatures. Exoplanet data are taken from Cadieux et al. (2024). Transonic mass loss rates are proportional to sonic-point densities (Eqn 38).

such that the transport equation for N becomes

$$\frac{F_{\text{XUV}} \bar{\sigma}_{\nu_I}}{h \bar{\nu}_I} n_N \approx n_e \alpha_{\text{RR}} n_{\text{N}^+} + n u \frac{df_+}{dr}, \quad (36)$$

where $f_+ = \frac{n_{\text{N}^+}}{n}$ and we have implemented a monochromatic approximation at the front (e.g., Murray-Clay et al. 2009). The mean of energy of photons producing singly and doubly ionised nitrogen is $h \bar{\nu}_I \approx 33.6 \text{ eV}$ and $h \bar{\nu}_{\text{II}} \approx 56.5 \text{ eV}$, and the mean absorption cross section are similar: $\bar{\sigma}_{\nu_I} \approx \bar{\sigma}_{\nu_{\text{II}}} \approx 10^{-17} \text{ cm}^2$ evaluated for a Modern Active Sun Spectrum (Huebner & Mukherjee 2015).

The cooling from the forbidden line cooling of NI and NII must balance the net heating from photoionisation:

$$n \epsilon F_{\text{XUV}}^\theta \left(f_+ \frac{\Delta \nu_{\text{II}}}{\bar{\nu}_{\text{II}}} \bar{\sigma}_{\nu_{\text{II}}} + (1 - f_+) \frac{\Delta \nu_I}{\bar{\nu}_I} \bar{\sigma}_{\nu_I} \right) \approx \sum_{\text{NI}}^{\text{NII}} \sum_{j,i>j}^{1 \rightarrow 3} n_i(T, n_e) A_{ij} E_{ij}, \quad (37)$$

where the average excess energies $\Delta \nu_{\text{I,II}} = \bar{\nu}_{\text{I,II}} - 3k_B T_e / 2 - h \nu_{\text{I,II}}$ and the number densities $n_i(T, n_e)$ are solutions from the three-level model (Eqn 29). The efficiency prefactor ϵ is the fraction of local heating sunk

into line cooling, as opposed to advection Q_{adv} and conduction Q_{cond} . Minor optical attenuation is also represented in $\epsilon \approx e^{-\tau}(1 - (Q_{\text{cond}} + Q_{\text{adv}})/Q_{\text{XUV}})$, where $\tau \lesssim 1$. Even if advection is major for the transport of ions, it may have a minor contribution to the energy balance. Thermal conduction down the thermospheric inversion can contribute significant cooling locally, but the front may also be found where the temperature profile has flattened. Thus, ϵ takes values $\sim 0.1 - 1$.

The collisional-radiative thermostat effect of Equation (37) is illustrated in Figure 10. For fixed electron density, order of magnitude changes in the XUV flux cause order unity changes in the temperature generated. However, higher XUV flux results in a greater electron density in the front, which increases line cooling and feedbacks on the temperature; see forced-hydrostatic evolution (black arrow, Fig 10). Optically thin absorption is proportional to the electron density (via the total density), while the line cooling dependence has a proportionality closer to the square of the electron density, which is exact in the two-level coronal model (Eqn 26b). Increasing electron density has a more marginal effect when approaching the critical density for LTE (see Sec 4.1), which is sometimes referred to as quenching (Bauer & Lammer 2004). For the transonic outflow equilibria, the mass loss rate can be interpolated from Figure 10 using

$$\Phi_{\text{hyd}} \simeq 4\pi r_{\text{sc}}^2 m(n_e/f_+) \sqrt{k_B T_{\text{sc}}/\mu}. \quad (38)$$

5.4. Comparison to Nakayama et al. (2022)

The collisional-radiative thermostat (Eqn 37) offers a broad physical explanation of the surprisingly uniform temperature dynamics of the exobase at high XUV fluxes in Nakayama et al. (2022): a feedback between forbidden line cooling and photoionisation heating mediated by electron density. Nakayama et al. (2022) calculate that for $500F_{\text{XUV},\oplus}$ the ionisation front $f_+ = 0.5$ occurs at an altitude of ~ 3000 km, reaching a peak temperature of 5500 K. The ionisation front temperatures for $50 \rightarrow 1000F_{\text{XUV},\oplus}$ are within a 500 K temperature interval, indicating a thermostatic effect must be present. In Figure 10, we explore a reduced model of the ionization with the forced hydrostatic arrow taking the range $(\epsilon F_{\text{XUV}}, n, f_e) : (30, 10^6 \text{ cm}^{-3}, 0.5) \rightarrow (300, 10^7 \text{ cm}^{-3}, 0.5)$. Equation 37 yields $T_{\text{stat}} : 6000 \rightarrow 8000$ K and above the front ionization fractions reach unity. Compared to Nakayama et al. (2022), the excess temperature can be partially explained through oxygen line cooling, which is neglected in our model.

However, the present study does not concur with Nakayama et al. (2022) that the thermostat allows survival of an Earth-like atmosphere up to $1000F_{\text{XUV},\oplus}$. Though the forced-hydrostatic Earth-like equilibrium in Figure 10 remains at less than half of the fixed-neutral escape temperature, it is the plasma escape temperature that should be considered for ionization fractions close to unity (Eqn 34). The forced-hydrostatic evolution in Figure 10 exceeds half the plasma escape temperature, almost reaching it, and would outflow. In general, the intermediate free evolution from hydrostatic instability to hydrodynamic escape could occur through the Coulomb-collisional expansion of ions and electrons aloft of a neutral N-exobase, which drags the atmosphere through the exobase in a drifting Maxwellian (Volkov 2011).

We also highlight the apparent lack of sensitivity of the height of the model exobase to increasing XUV flux in Nakayama et al. (2022). On the flux increasing by a factor of ten from $50 \rightarrow 500F_{\text{XUV},\oplus}$, the apparent height increases only by 20%. We expect that the increase of peak electron density with XUV flux should push the exobase significantly further out because (1) the scale height increases with the reduction of mean molecular weight from ambipolar diffusion and (2) the more frequent electron-neutral and ion-neutral collisions allow the neutral-N exobase to form at orders of magnitude lower densities. Moreover, at $500F_{\text{XUV},\oplus}$ Nakayama et al. (2022) find the ionization fraction at the top of the atmosphere to be unity, so that before the mean free path of nitrogen atoms grow large enough for ballistic escape, the atmosphere is ionized enough that formation of a neutral exobase is precluded.

The polytropic model and the transonic onset equilibrium for Young-Sun Earth in Figure 10 roughly agree that $400F_{\text{XUV},\oplus}$ provides enough heating to drive escape at the neutral onset as a conservative estimate. So, together with the instability of the forced hydrostatic equilibrium (Fig 10) relative to the plasma escape temperature, our idealized modeling offers a consistent picture.

5.5. TRAPPIST 1-b: Airless

TRAPPIST-1 b has radius $1.16R_{\oplus}$ and mass $1.37M_{\oplus}$ (Agol et al. 2021). Its escape velocity is then 12.2 km s^{-1} , less than 10 % different from Earth, so we expect a similar escape regime for similar XUV fluxes. We do not plot TRAPPIST-1 b's escape temperatures in Figure 10 because they are similar to Earth's.

During the superluminous phase of TRAPPIST-1, the XUV flux received by the closest in planet 'b' may have been $10^4 - 10^5 \times F_{\text{XUV},\oplus}$ (Fleming et al. 2020). In that case, a hypothetical atmospheric outflow of nitrogen might occupy the $(\epsilon F_{\text{XUV}}, n, f_+) : (10^{3.5} -$

Table 2: Equilibria of Photoevaporating Nitrogen Atmospheres

<i>Transonic:</i>	$\times F_{\text{XUV},\oplus}$	Vertical eqm	Primary balance	f_+	Consistent	Comment	Φ_{hyd} (bar/MYr)
YS Mars	50	hydrodynamic	ionization-advection	$\lesssim 0.1$	✓	$q_\gamma \gg q_c$, EL	20
YS Earth	400	hydrostatic	ionization-recombination	$\lesssim 1$	×	\rightarrow ion outflow	
		hydrodynamic	ionization-advection	~ 0.1	✓*	$q_\gamma \gtrsim q_c$	6
LHS-1140 c	1000	hydrodynamic	ioniz.-adv.-recom.	~ 1	✓(?)	$1.9 \times M_\oplus$, EL	~ 0.4
LHS-1140 b	2000	hydrodynamic	ioniz.-adv.-recom.	~ 1	✓(?)	$5.6 \times M_\oplus$, EL	~ 0.6

NOTE—Note the following: YS stands for the Young Sun scenarios modeled. q_γ and q_c refer to local XUV-heating and atomic line cooling with altitude. EL refers to following the energy-limit with the caveat of the onset and ~~EL~~ refers to the energy limit breaking down and the collisional radiative thermostat. The transition to (\rightarrow) ion outflow refers to transient evolution from an unstable hydrostatic atmosphere. The abbreviation ioniz.-adv.-recom. refers to ionization balanced by advection and recombination as for the steady state of global ion outflow. Numbers are based on the analytic modeling reported in the present study. This table of best guesses requires follow-up work with hydrocodes and DSMC simulations.

10^4 , 10^7cm^{-3} , 1) with a close-in sonic point, possibly a detached D-type shock (Spitzer 1978). The dominant balance of photoionization is then likely to be from radiative recombination, which has been considered in the photoevaporation of hydrogen envelopes (e.g., Murray-Clay et al. 2009; Owen & Jackson 2012). However, the physics for recombination-limited outflows of a ‘metal’ atmosphere differs strongly, so the scaling derived by Murray-Clay et al. (2009) is not expected to hold.

We do not include an equilibrium on Figure 10 nor a row in Table 2 for this escape as it would be catastrophic; unlikely to be consistent with a relevant steady state. Instead, any outgassing would not be able to form a secondary atmosphere on TRAPPIST-1 b until after the saturated phase, and even then it would still be receiving greater than Young-Sun Earth fluxes, so it is unlikely a secondary atmosphere could ever form. Van Looveren et al. (2024) calculate that even the present-day fluxes of ionizing radiation in the TRAPPIST-1 planetary system are intense enough to preclude the retention of any secondary atmospheres. However, we note that they use a forced-hydrostatic Jeans prescription of escape that does not include the key electric-dipole-forbidden lines.

5.6. LHS-1140 b and c: Airy?

The escape temperature for a predominantly neutral flow from LHS-1140 c ($1.9M_\oplus$, $1.27R_\oplus$, 0.027 AU) would be $\gtrsim 22\,000$ K due to the $1.5\times$ tighter gravitational binding than of Earth. However, temperatures would be kept lower by the collisional-radiative thermostat under rising XUV fluxes even for $> 1000 \times F_{\text{XUV},\oplus}$, so transonic escape with a significant neutral fraction is prevented. The ion-acoustic speed in an ion outflow allows the plasma escape temperature to be half as large as the neutral.

The pink cross in Figure 10 explores a hypothetical sonic point with an electron density of 10^5cm^{-3} requiring an XUV flux of $\sim 10^3 F_{\text{XUV},\oplus}$ if $\epsilon \sim 0.5$. The mass loss rate would then be around a bar per two million years. So, escape would not be driven for LHS-1140 c with its contemporary instellation of $10^2 F_{\text{XUV},\oplus}$ (Spinelli et al. 2023), but a secondary atmosphere formed in the early pre-main-sequence with $\gtrsim 10^3 \times F_{\text{XUV},\oplus}$ could well have been lost.

The companion planet LHS-1140 b ($5.6M_\oplus$, $1.7R_\oplus$, 0.09 AU) has a $3\times$ deeper gravitational well than Earth, so the neutral escape temperature would be in the ballpark of $\gtrsim 50\,000$ K. As a result, only an ion outflow is feasible for the hydrodynamic escape of a secondary atmosphere from a ‘radius valley’ planet. Inspecting the green cross in Figure 10, even if the sonic point could form as far out as $4.5R_{\text{pl}}$, then assuming $\epsilon \sim 0.5$ and an electron density 10^5cm^{-3} an XUV flux of $2000 F_{\text{XUV},\oplus}$ would be required. At lower densities the flux required would be reduced but so would the escape rate (Eqn 38). In the LHS-1140 system, planet b only receives one twelfth of the instellation of c. So, a thick secondary atmosphere is unlikely to be photoevaporated even accounting early pre-main-sequence fluxes.

So, whether LHS-1140 c would retain a thick secondary atmosphere will be sensitive to its initial conditions but LHS-1140 b should have retained its atmosphere, as consistent with observations from Cadieux et al. (2024). For cool rocky planets orbiting low-mass stars, the higher escape temperatures of super-Earths compared to sub-Earths is crucial to prospects for the retention of secondary atmospheres.

6. DISCUSSION

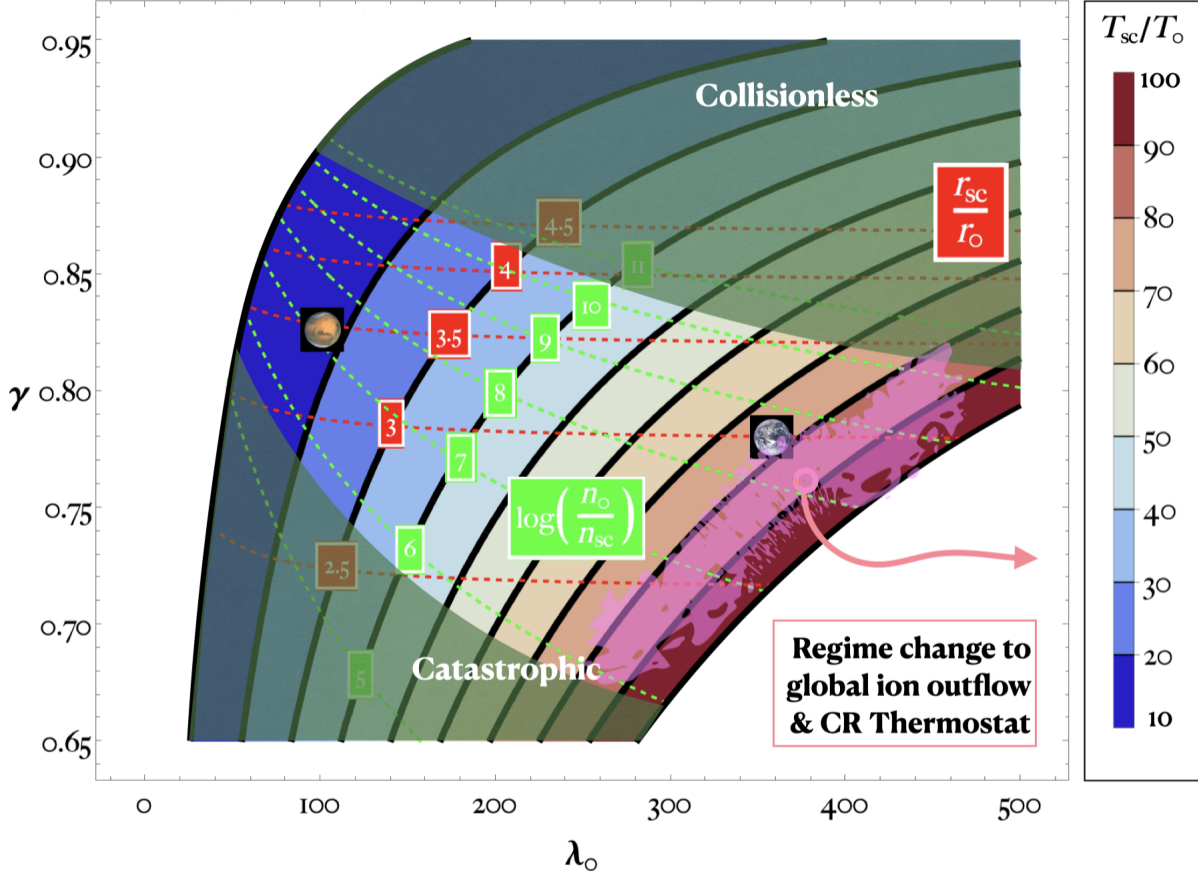


Figure 11: Regime diagram for high molecular weight escape in terms of the polytropic index $0.65 \leq \gamma \leq 0.95$ and the hydrodynamic escape parameter $10 \leq \lambda_0 \leq 400$. The heat map indicates the ratio of sonic to base temperatures 10 – 100. Contours of uniform ratio of sonic to base radius (red-dashed) and uniform sonic to base density in log units (green dashed). The Young Sun Earth (c.f. Figures 4 & 8B) and Young Sun Mars (see Figures 5 & 8A) calculations are represented by images of each planet. This figure can be compared to the solution space of polytropic solutions (Fig 3). For large enough λ_0 , the polytropic model of steep XUV inversions breaks down because line cooling will begin to dominate over advection. The overlaying pink patch is to illustrate that the shift is broad and dependent on boundary conditions and dimensional parameters. Rightward of the transition, the collisional radiative thermostat will control the resulting global ion outflow (see Section 5).

The rapid escape of heavier species is usually only considered in drag-off by hydrogen, so the direct hydrodynamic escape of a nitrogen or carbon dioxide atmosphere is often left out of atmospheric evolution studies of rocky planets (e.g., Teixeira et al. 2023). In fact, for a planet with a thick secondary atmosphere, such as Venus, other erosion mechanisms are generally too slow or variable, leaving direct hydrodynamic escape as the main route to airlessness (e.g., Gronoff et al. 2020). Early *JWST* observations are revealing a pattern of cool rocky worlds that are airless or thinly blanketed. Thus, observations and theory suggest that atmospheric retention could be a major bottleneck in the occurrence of observable Earth-like habitats η_{\oplus} (e.g., Scherf et al. 2022).

6.1. Landscape of High Molecular Weight Escape

The polytropic framework allows a comparative planetology perspective, with the resulting insight resolvable into the simplified representation of the range of governing physics. Figure 11 has λ_0 on the vertical axis: the ratio of gravitational binding to the thermal reservoir at the mesopause. On the horizontal axis is γ describing the steepness of the temperature inversion, which is implicitly determined by XUV instellation (Eqn 20). Ratios of base to sonic densities, temperatures, and radii can be read from Figure 11. The diagram can be used as a visual aid to see for which star-planet conditions hydrodynamic escape will be possible.

The pairwise base-to-sonic ratios in log units map to the proportionally varying Knudsen number at the sonic point if holding base density constant. The right-hand

edge where collisional onset may be possible is roughly marked as where the sonic density is ten orders of magnitude smaller than at the base. On the $\log [n_0/n_{sc}] = 10$ contour itself, extremely deep penetration of XUV would be required flow to launch the outflow from that dense portion of the atmosphere. The left-hand edge is given by the $\log [n_0/n_{sc}] = 6$ contour, where the sonic Knudsen number would likely be more than an order of magnitude smaller than at onset. In this high XUV-flux limit, the assumption of predominantly neutral outflow is likely to break down. Furthermore, the mass loss will be catastrophically fast.

In the region marked out between $6 < \log [n_0/n_{sc}] < 10$, the sonic radii vary between two and four times the planetary radius. The base to sonic temperature ratio is given by $T_{sc} = \frac{\lambda_0 r_0 T_0}{2\gamma r_{sc}}$, and is a proxy for when line cooling will become significant in the atmospheres of temperate rocky planets. Accordingly, the consistency of transonic hydrodynamic escape is clear-cut for XUV-evaporation of a thick nitrogen atmosphere on a Mars-like planet due to the lower gravitational binding of the atmosphere. Transonic hydrodynamic escape of the nitrogen atmosphere can be driven with upper atmosphere temperatures staying below 4000K, low enough for negligible line cooling. The threshold XUV flux for collisional onset for Mars is calculated as $100\times$ Modern Day Mars XUV, which we highlight as overly conservative compared to previous studies (e.g., Tian et al. 2009), and would entail a rapid loss rate of 20 bars per million years. For much lower XUV fluxes, the threshold for instability of a hydrostatic nitrogen atmosphere at ~ 2000 K would be exceeded.

For the gravitational binding of the Earth's atmosphere and a cool mesopause, the temperatures monotonically increased to roughly 19000 K at the sonic point at Knudsen neutral onset. Auroral line cooling from $[\text{NI}]_{1.04\mu\text{m}}^{3\rightarrow 2}$ and $[\text{NII}]_{611\text{nm}}^{3\rightarrow 2}$ almost matches the polytropic heating regionally. Accounting for line cooling through $\eta_c = 0.5$ in the energy limit (Eqns 6 and 7b), we find the hydrodynamic loss of six bars of nitrogen per million years for $400\times$ Modern Day Solar XUV irradiation. To build confidence in this result, we checked agreement from opposite perspective of the line cooling balancing XUV heating with advection being an efficiency factor. We also reanalyzed the hydrostatic thermosphere profiles of Nakayama et al. (2022), finding instability at $500F_{\text{XUV},\oplus}$, possibly lower, while accounting for the effect of ion-electron interactions on the mean molecular weight as captured by the plasma escape temperature (Section 5.1). Earth can be viewed as occupying yet another sweet spot where the energy limit starts to break

down, and the collisional-radiative thermostat takes over for the loss of secondary atmospheres.

The upper-atmosphere temperatures required to rapidly escape planetary atmospheres with gravitational binding greater than Earth's are prohibitive for the case of predominantly neutral outflow. We hypothesize that even higher XUV fluxes can instead lead to global ion outflow, with atomic line cooling controlling the rate of escape and the collisional regime extending to greater altitudes. Accordingly, a steep polytropic inversion from the thermobase is a poor model. This is highlighted with the righthand regime change in Figure 11.

An onset of rapid escape can be found by matching the collisional-radiative thermostated sonic point with the plasma escape temperature, which is more easily achieved due to the twice-as-fast ion-acoustic sound speed (Eqn 31). The plasma escape temperature of the super-Earth LHS-1140 c ($1.9M_{\oplus}$) at three planetary radii is roughly 13000 K. Sonic point analysis suggests an uncertain mass loss rate of several bars of nitrogen in ten million years on exposure to $\sim 10^3 F_{\text{XUV},\oplus}$ (Figure 10). However, more detailed modeling is required to characterize the super-Earth regime beyond the result that escape is appreciably more difficult than from Earth and should take the form of an ion outflow.

Overall, within model uncertainty, Modern Earth's atmosphere might well survive in the XUV-irradiation environment of the Young Sun, depending on its initial rotation rate. However, if placed in the habitable zone of an active M-dwarf, our analysis suggests that the protective effect of the line cooling is overwhelmed, and a thick secondary atmosphere would likely be lost. Thus, from the perspective of escape, no substantial atmospheres are expected on the TRAPPIST-1 planets. More advanced modeling and more observations will constrain the reality. For super-Earths orbiting M-dwarfs, the zone of atmospheric retention is larger, making them the most promising observational targets for detecting features of an Earth-like habitat.

6.2. Cosmic Shoreline for Rocky Exoplanets

The emerging dynamics of the work reported here suggests a non-uniform trend for separating airless and airy planets in the space of XUV flux/fluence against a power law in escape velocity. We venture to make some broad predictions for the cosmic shoreline in contrast with Zahnle & Catling (2017). The nonlinear onset and rapid rates of transonic outflow suggest that the key parameter governing the escape of secondary atmospheres is the peak XUV flux experienced at different ages, rather than the lifetime fluence:

- I. A star’s X-ray luminosity is enhanced $3\times$ above the long-term average at each evolutionary stage for 10% of the time (Johnstone et al. 2021). So, if the *average* main-sequence XUV flux is greater than one third of the threshold for transonic escape, a secondary atmosphere is unlikely to survive or be revived.
- II. Otherwise, if main sequence XUV fluxes are low enough that a secondary atmosphere would remain hydrostatic throughout, then its survival will depend on an interplay between stellar wind erosion, volcanic activity and impacts (Kite & Barnett 2020).
- III. Accretion of an envelop of nebular hydrogen, by weathering some or all of the saturated phase of coronal activity on the pre-main-sequence, enhances prospects for retention of Earth-like or Venus-like atmosphere. However, where significant metals are lost in hydrogen escape, or the saturated phase last long enough to escape hydrogen and residual secondary components, then the mantle could be catastrophically depleted in volatiles, precluding later revival.
- IV. We expect the sub-Earth and super-Earth regimes to present as a two-part cosmic shoreline. For rocky planets with escape velocities larger than Earth’s, the escape rate and threshold XUV flux are governed by the collisional-radiative thermostat, whereas for smaller escape velocities, the rates are energy-limited with a Knudsen onset.

Model mass losses for a range of planets spanning the cosmic shoreline are summarised in Table 2. The large XUV flux requirements for transonic escape could be relaxed in the case of significant Joule heating (Cohen et al. 2024). Both sides of the cosmic shoreline are tentatively being populated (e.g., Diamond-Lowe et al. 2020; Mansfield et al. 2024; Xue et al. 2024; Cadieux et al. 2024). We hope the present study can aid in making population-level predictions for the retention of rocky exoplanet atmospheres.

7. SUMMARY

We conclude that the escape rate of secondary atmospheres from Mars-to-Earth-sized bodies can be roughly calculated with an energy limit above a threshold XUV flux given by the Knudsen-onset in collisionality at the sonic point. For super-Earths, escape shifts towards a transonic global ion outflow with the thermal structure determined by the balance of photoionisation heating and forbidden line cooling. The transonic onset and escape rate can be roughly interpolated from the collisional-radiative thermostat presented in Figure 10.

These results are consistent with the vulnerability of TRAPPIST-1 b and c to easily lose a thick atmosphere and for LHS-1140 b to hold on to a possibly N_2 -dominated secondary atmosphere.

We explored the landscape of high molecular weight escape (see Figure 11) by varying the power-law index γ corresponding to the steepness of atmospheric inversion driven by idealised XUV heating. Given the gravitational binding of the atmosphere described by escape parameter λ_0 , analytic solutions to the atmospheric profiles were found, including approximations for the sonic-point properties and thermomechanical efficiency, which are relatively insensitive to a physically motivated range of lower boundary conditions. We compared our Young-Sun Earth transonic escape model with hydrocode simulations from Johnstone et al. (2019).

We diagnosed forbidden-line cooling from polytropic profiles with a three-level atom model, finding it minor for Young-Sun Mars transonic escape and significant for Young-Sun Earth. We develop an explanation for the temperature behavior in varying XUV fluxes of Nakayama et al. (2022) based on the feedback from electron densities on the forbidden line cooling in the photoionization front. We generalize the notion, calling it the collisional-radiative thermostat, and explore its control on escape under a range of conditions.

For strongly ionized atmospheres, the ambipolar electric field halves the mean molecular weight compared to a predominantly neutral flow, reducing the temperatures required for hydrostatic instability and transonic outflow by half. We suggest that incomplete accounting of these ion-electron interactions explains how Nakayama et al. (2022) find persistent stability even up to $1000\times$ Modern Earth XUV fluxes, in contrast with our study, which finds transonic outflow for half that flux or less. We propose that the shift to ion-acoustic sound speed, characterized by the *plasma* escape temperature, allows the transonic outflow of a secondary atmosphere from a super-Earth even under the action of the collisional-radiative thermostat (see Figure 10).

The work reported here marks the first 1D analytic modeling of the XUV-driven transonic escape of secondary atmospheres from rocky exoplanets. Our inclusion of both ion-electron effects and forbidden-line cooling sets a precedent for modeling global loss of secondary atmospheres. Future studies involving state-of-the-art photochemistry, self-consistent hydrodynamics, and Direct simulation Monte Carlo methods will be crucial in theoretically constraining Eta-Earth and the Cosmic Shoreline.

Software: Mathematica 14.1 (Wolfram Research 2024)

R.D.C thanks Hamish Innes and Antonio García Muñoz for providing feedback on the manuscript, Sarah Blumenthal for advice on photochemistry and Robert

E. Johnson for interesting discussions. We thank the anonymous reviewer for comments that greatly improved the manuscript. This work was supported by the Science and Technology Facilities Council (STFC) and the Alfred P. Sloan Foundation under grant G202114194 (AETHER).

REFERENCES

- Agol, E., Dorn, C., Grimm, S. L., et al. 2021, *PSJ*, 2, 1, doi: [10.3847/PSJ/abd022](https://doi.org/10.3847/PSJ/abd022)
- Badnell, N. R. 2006, *ApJS*, 167, 334, doi: [10.1086/508465](https://doi.org/10.1086/508465)
- Bauer, A., & Carter, P. 2021, *SIAM Journal on Applied Dynamical Systems*, 20, 262, doi: [10.1137/20M1314240](https://doi.org/10.1137/20M1314240)
- Bauer, S., & Lammer, H. 2004, *Planetary Aeronomy, Atmosphere Environments in Planetary Systems* (Springer), doi: [10.1007/978-3-662-09362-7](https://doi.org/10.1007/978-3-662-09362-7)
- Bird, G. 1994, *Molecular Gas Dynamics and the Direct Simulation of Gas Flows* (Clarendon Press)
- Cadieux, C., Doyon, R., MacDonald, R. J., et al. 2024, *ApJL*, 970, L2, doi: [10.3847/2041-8213/ad5afa](https://doi.org/10.3847/2041-8213/ad5afa)
- Catling, D., & Kasting, J. 2017, *Atmospheric evolution on inhabited and lifeless worlds* (CUP)
- Chandrasekhar, S. 1931, *ApJ*, 74, 81, doi: [10.1086/143324](https://doi.org/10.1086/143324)
- Chen, F. F. 2016, *Introduction to Plasma Physics and Controlled Fusion* (Springer International Publishing)
- Cohen, O., Glocer, A., Garraffo, C., et al. 2024, *ApJ*, 962, 157, doi: [10.3847/1538-4357/ad206a](https://doi.org/10.3847/1538-4357/ad206a)
- Collinson, G. A., Glocer, A., Pfaff, R., et al. 2024, *Nature*, 632, 1021, doi: [10.1038/s41586-024-07480-3](https://doi.org/10.1038/s41586-024-07480-3)
- Cranmer, S. R. 2004, *AmJPh*, 72, 1397, doi: [10.1119/1.1775242](https://doi.org/10.1119/1.1775242)
- Diamond-Lowe, H., Charbonneau, D., Malik, M., Kempton, E. M.-R., & Beletsky, Y. 2020, *AJ*, 160, 188, doi: [10.3847/1538-3881/abaf4f](https://doi.org/10.3847/1538-3881/abaf4f)
- Dressing, C. D., & Charbonneau, D. 2015, *ApJ*, 807, 45, doi: [10.1088/0004-637X/807/1/45](https://doi.org/10.1088/0004-637X/807/1/45)
- Drew, J. E. 1985, *MNRAS*, 217, 867, doi: [10.1093/mnras/217.4.867](https://doi.org/10.1093/mnras/217.4.867)
- Erwin, J., Tucker, O., & Johnson, R. E. 2013, *Icarus*, 226, 375, doi: <https://doi.org/10.1016/j.icarus.2013.05.042>
- Ferland, G. J., Fabian, A. C., Hatch, N. A., et al. 2009, *MNRAS*, 392, 1475, doi: [10.1111/j.1365-2966.2008.14153.x](https://doi.org/10.1111/j.1365-2966.2008.14153.x)
- Feynman, R. P., Leighton, R. B., & Sands, M. 2011, *The Feynman lectures on physics, Vol. I: The new millennium edition: mainly mechanics, radiation, and heat*
- Fleming, D. P., Barnes, R., Luger, R., & VanderPlas, J. T. 2020, *ApJ*, 891, 155, doi: [10.3847/1538-4357/ab77ad](https://doi.org/10.3847/1538-4357/ab77ad)
- Fulton, B. J., Petigura, E. A., Howard, A. W., et al. 2017, *AJ*, 154, 109, doi: [10.3847/1538-3881/aa80eb](https://doi.org/10.3847/1538-3881/aa80eb)
- García Muñoz, A., Asensio Ramos, A., & Faure, A. 2024, *Icarus*, 415, 116080, doi: <https://doi.org/10.1016/j.icarus.2024.116080>
- Gillon, M., Triaud, A. H. M. J., Demory, B.-O., et al. 2017, *Nature*, 542, 456, doi: [10.1038/nature21360](https://doi.org/10.1038/nature21360)
- Goldsmith, P. F., Yildiz, U. A., Langer, W. D., & Pineda, J. L. 2015, *Astrophysical Journal*, 814, doi: [10.1088/0004-637X/814/2/133](https://doi.org/10.1088/0004-637X/814/2/133)
- Greene, T. P., Bell, T. J., Ducrot, E., et al. 2023, *Nature*, 618, 39, doi: [10.1038/s41586-023-05951-7](https://doi.org/10.1038/s41586-023-05951-7)
- Gronoff, G., Arras, P., Baraka, S., et al. 2020, *JGRA*, 125, doi: <https://doi.org/10.1029/2019JA027639>
- Heays, Bosman, A. D., & van Dishoeck, E. F. 2017, *A&A*, 602, A105, doi: [10.1051/0004-6361/201628742](https://doi.org/10.1051/0004-6361/201628742)
- Holzer, T. E., & Axford, W. I. 1970, *ARA&A*, 8, 31, doi: <https://doi.org/10.1146/annurev.aa.08.090170.000335>
- Hong, J. M., Yen, C. C., & Huang, B. C. 2014, *SJADS*, 74, 1709, doi: [10.1137/130919957](https://doi.org/10.1137/130919957)
- Hu, R., & Thomas, T. B. 2022, *Nature Geoscience*, 15, 106, doi: [10.1038/s41561-021-00886-y](https://doi.org/10.1038/s41561-021-00886-y)
- Huang, S.-S. 1959, *PASP*, 71, 421, doi: [10.1086/127417](https://doi.org/10.1086/127417)
- Huebner, W. F., & Mukherjee, J. 2015, *P&SS*, 106, 11, doi: [10.1016/j.pss.2014.11.022](https://doi.org/10.1016/j.pss.2014.11.022)
- Jeans, J. H. 1921, *The dynamical theory of gases* (University Press)
- Johnson, R. E., Volkov, A. N., & Erwin, J. T. 2013a, *ApJL*, 768, L4, doi: [10.1088/2041-8205/768/1/L4](https://doi.org/10.1088/2041-8205/768/1/L4)
- . 2013b, *ApJL*, 779, L30, doi: [10.1088/2041-8205/779/2/L30](https://doi.org/10.1088/2041-8205/779/2/L30)
- Johnstone, Khodachenko, M. L., Lüftinger, T., et al. 2019, *A&A*, 624, L10, doi: [10.1051/0004-6361/201935279](https://doi.org/10.1051/0004-6361/201935279)
- Johnstone, C. P. 2020, *ApJ*, 890, 79, doi: [10.3847/1538-4357/ab6224](https://doi.org/10.3847/1538-4357/ab6224)
- Johnstone, C. P., Bartel, M., & Güdel, M. 2021, *A&A*, 649, A96, doi: [10.1051/0004-6361/202038407](https://doi.org/10.1051/0004-6361/202038407)
- Kislyakova, Holmström, M., Odert, P., et al. 2019, *A&A*, 623, A131, doi: [10.1051/0004-6361/201833941](https://doi.org/10.1051/0004-6361/201833941)
- Kite, E. S., & Barnett, M. N. 2020, *PNAS*, doi: [10.1073/pnas.2006177117/-/DCSupplemental](https://doi.org/10.1073/pnas.2006177117/-/DCSupplemental)

- Knudsen, M. 1909, *AnP*, 333, 75,
doi: [10.1002/andp.19093330106](https://doi.org/10.1002/andp.19093330106)
- Koskinen, T., Harris, M., Yelle, R., & Lavvas, P. 2013, *Icarus*, 226, 1678,
doi: <https://doi.org/10.1016/j.icarus.2012.09.027>
- Krissansen-Totton, J., Wogan, N., Thompson, M., & Fortney, J. J. 2024, *Nature communications*, 15, 8374,
doi: [10.1038/s41467-024-52642-6](https://doi.org/10.1038/s41467-024-52642-6)
- Kubyshkina, D., Fossati, L., Erkaev, N. V., et al. 2018, *The Astrophysical Journal Letters*, 866, L18,
doi: [10.3847/2041-8213/aae586](https://doi.org/10.3847/2041-8213/aae586)
- Kunc, J. A., & Soon, W. H. 1989
- Lamers, H., & Cassinelli, J. 1999, *Introduction to Stellar Winds* (Cambridge University Press)
- Lammer, H., Sproß, L., Grenfell, J. L., et al. 2019, *Astrobiology*, 19, 927, doi: [10.1089/ast.2018.1914](https://doi.org/10.1089/ast.2018.1914)
- Lammer, H., Zerkle, A. L., Gebauer, S., et al. 2018, *Astronomy and Astrophysics Review*, 26,
doi: [10.1007/s00159-018-0108-y](https://doi.org/10.1007/s00159-018-0108-y)
- Laricchiuta, A., Bruno, D., Capitelli, M., et al. 2009, *EPJD*, 54, 607, doi: [10.1140/epjd/e2009-00192-7](https://doi.org/10.1140/epjd/e2009-00192-7)
- Lopez, E. D., & Fortney, J. J. 2013, *ApJ*, 776, 2,
doi: [10.1088/0004-637X/776/1/2](https://doi.org/10.1088/0004-637X/776/1/2)
- López-Puertas, M., & Taylor, F. W. 2001, *Non-LTE Radiative Transfer in the Atmosphere* (World Scientific)
- Mansfield, M. W., Xue, Q., Zhang, M., et al. 2024,
<https://arxiv.org/abs/2408.15123>
- Murray-Clay, R. A., Chiang, E. I., & Murray, N. 2009, *ApJ*, 693, 23, doi: [10.1088/0004-637x/693/1/23](https://doi.org/10.1088/0004-637x/693/1/23)
- Nakayama, A., Ikoma, M., & Terada, N. 2022, *ApJ*, 937, 72, doi: [10.3847/1538-4357/ac86ca](https://doi.org/10.3847/1538-4357/ac86ca)
- Owen, J. E., & Jackson, A. P. 2012, *MNRAS*, 425, 2931,
doi: [10.1111/j.1365-2966.2012.21481.x](https://doi.org/10.1111/j.1365-2966.2012.21481.x)
- Owen, J. E., & Wu, Y. 2013, *ApJ*, 775, 105,
doi: [10.1088/0004-637X/775/2/105](https://doi.org/10.1088/0004-637X/775/2/105)
- Parker, E. N. 1958, *ApJ*, 128, doi: [10.1086/146579](https://doi.org/10.1086/146579)
- Pierrehumbert, R. T. 2010, *Principles of Planetary Climate* (CUP), doi: [10.1017/CBO9780511780783](https://doi.org/10.1017/CBO9780511780783)
- Ribas, I., Guinan, E. F., Güdel, M., & Audard, M. 2005, *ApJ*, 622, 680, doi: [10.1086/427977](https://doi.org/10.1086/427977)
- Scherf, M., Lammer, H., & Sproß, L. 2022, in *EPSC 2022, Granada*, doi: [10.5194/epsc2022-1032](https://doi.org/10.5194/epsc2022-1032)
- Seaton, M. J. 1960, *RPPH*, 23, 313,
doi: [10.1088/0034-4885/23/1/306](https://doi.org/10.1088/0034-4885/23/1/306)
- Solomon, S. C. 2010, *Terrestrial ionospheres* (Cambridge University Press), 351–362
- Spinelli, R., Gallo, E., Haardt, F., et al. 2023, *AJ*, 165, 200,
doi: [10.3847/1538-3881/acc336](https://doi.org/10.3847/1538-3881/acc336)
- Spitzer, L. J. 1978, *Physical processes in the interstellar medium* (Wiley), doi: [10.1002/9783527617722](https://doi.org/10.1002/9783527617722)
- Tang, Y., Fortney, J. J., & Murray-Clay, R. 2024, *ApJ*, 976, 221, doi: [10.3847/1538-4357/ad8567](https://doi.org/10.3847/1538-4357/ad8567)
- Teixeira, K. E., Morley, C. V., Foley, B. J., & Unterborn, C. T. 2023, *ApJ*, 960, 44, doi: [10.3847/1538-4357/ad0cec](https://doi.org/10.3847/1538-4357/ad0cec)
- Tian, F. 2009, *ApJ*, 703, 905,
doi: [10.1088/0004-637X/703/1/905](https://doi.org/10.1088/0004-637X/703/1/905)
- Tian, F., Kasting, J. F., Liu, H. L., & Roble, R. G. 2008, *JGRE*, 113, doi: [10.1029/2007JE002946](https://doi.org/10.1029/2007JE002946)
- Tian, F., Kasting, J. F., & Solomon, S. C. 2009, *GRL*, 36,
doi: [10.1029/2008GL036513](https://doi.org/10.1029/2008GL036513)
- Tucker, W. H., & Gould, R. J. 1966, *ApJ*, 144, 244,
doi: [10.1086/148601](https://doi.org/10.1086/148601)
- Van Looveren, G., Güdel, M., Boro Saikia, S., & Kislyakova, K. 2024, *A&A*, doi: [10.1051/0004-6361/202348079](https://doi.org/10.1051/0004-6361/202348079)
- Velli, M. 1994, *ApJL*, 432, L55, doi: [10.1086/187510](https://doi.org/10.1086/187510)
- Vidal-Madjar, A., Des Etangs, A. L., Désert, J.-M., et al. 2003, *Nature*, 422, 143
- Vidal-Madjar, A., Dsert, J.-M., des Etangs, A. L., et al. 2004, *ApJ*, 604, L69, doi: [10.1086/383347](https://doi.org/10.1086/383347)
- Vilhu, O. 1984, *A&A*, 133, 117
- Volkov, A. N. 2011, *PhFl*, 23, doi: [10.1063/1.3592253](https://doi.org/10.1063/1.3592253)
- Watson, A. J., Donahue, T. M., & Ker, J. C. G. W. 1981, *Icarus*, 48, 150
- Wolfram Research, I. 2024, *Mathematica*, Version 14.1, Wolfram Research, Inc., Champaign, Illinois
- Xue, Q., Bean, J. L., Zhang, M., et al. 2024, *ApJL*, 973, L8,
doi: [10.3847/2041-8213/ad72e9](https://doi.org/10.3847/2041-8213/ad72e9)
- Yoshida, T., Terada, N., Ikoma, M., & Kuramoto, K. 2022, *ApJ*, 934, 137, doi: [10.3847/1538-4357/ac7be7](https://doi.org/10.3847/1538-4357/ac7be7)
- Zahnle, K. J., & Catling, D. C. 2017, *ApJ*, 843, 122,
doi: [10.3847/1538-4357/aa7846](https://doi.org/10.3847/1538-4357/aa7846)
- Zatsarinny, O., Gorczyca, T. W., Korista, K. T., Badnell, N. R., & Savin, D. W. 2004, *A&A*, 417, 1173,
doi: [10.1051/0004-6361:20034174](https://doi.org/10.1051/0004-6361:20034174)
- . 2005, *A&A*, 440, 1203,
doi: [10.1051/0004-6361:20034174e](https://doi.org/10.1051/0004-6361:20034174e)
- Zieba, S., Kreidberg, L., Ducrot, E., et al. 2023, *Nature*, 620, 746, doi: [10.1038/s41586-023-06232-z](https://doi.org/10.1038/s41586-023-06232-z)
- Öpik, E. J. 1963, *Geophysical Journal International*, 7, 490,
doi: [10.1111/j.1365-246X.1963.tb07091.x](https://doi.org/10.1111/j.1365-246X.1963.tb07091.x)